Fall 2019

Design and prototyping of a real-time millimeter wave imaging system

Zahra Manzoor

Department: Electrical and Computer Engineering

Recommended Citation

Manzoor, Zahra, "Design and prototyping of a real-time millimeter wave imaging system" (2019). *Doctoral Dissertations*. 2839.
https://scholarsmine.mst.edu/doctoral_dissertations/2839

DESIGN AND PROTOTYPING OF A REAL-TIME MILLIMETER WAVE IMAGING SYSTEM

by

ZAHRA MANZOOR

A DISSERTATION

Presented to the Faculty of the Graduate School of the

MISSOURI UNIVERSITY OF SCIENCE AND TECHNOLOGY

In Partial Fulfillment of the Requirements for the Degree

DOCTOR OF PHILOSOPHY

in

ELECTRICAL ENGINEERING

2019

Approved by:

Kristen Donnell, Advisor
Mohammad Tayeb Al Qaseer, Co-advisor
Reza Zoughi
Jie Huang
Xiaoming He

PUBLICATION DISSERTATION OPTION

This dissertation consists of the following three articles, formatted in the style used by the Missouri University of Science and Technology:

Paper I: Pages 8-32 have been submitted to IEEE Transactions on Antennas and Propagation.

Paper II: Pages 33-61 have been submitted to IEEE Transactions on Instrumentation & Measurement.

Paper III: Pages 62-94 have been submitted to IEEE Transactions on Antennas and Propagation.

ABSTRACT

The goal of this work is to design, prototype and test an innovative millimeter wave imaging system that operates in the frequency range of 33-35 GHz and is capable of producing rapid images of various diverse scenes. In particular, the imaging system includes two main sections, one is related to the hardware design of the system, and the other focuses on the development of a novel comprehensive image reconstruction algorithm. The hardware design includes custom transmitter and receiver sub-systems, and a sparse switched array which was optimized for 320 mm x 220 mm aperture plane, and also included an improved antipodal Vivaldi antenna featuring a substantial reduction in unwanted radiation as the array element. All aspects of the hardware system were simulated, prototyped and tested in this work prior to final system integration. As it relates to the reconstruction algorithm, traditionally bistatic imaging systems utilized an equivalent monostatic imaging algorithm. However, this leads to degradation in image quality. The level of this degradation was analyzed using image error metrics and conditions for minimum image error were obtained. Additionally, a robust amplitude compensated range migration algorithm (AC-RMA) was developed that is applicable for both bistatic and monosatic configurations. The AC-RMA is capable of successfully reconstructing target images independent of the dielectric contrast between the target and background, additive noise power, and bandwidth of the imaging system. In addition, while the formulation of the AC-RMA is more complicated than the traditional (phase compensation only) RMA, the processing time necessary for images created with the AC-RMA is just 1.2 times greater than that of the traditional RMA processing time.

ACKNOWLEDGMENTS

I would like to express my utmost gratitude to my advisor, Dr. Kristen M. Donnell and, Dr. Mohammad Tayeb Al Qaseer for their earnest support, inspirations, and the many hours they have devoted to me. Although this dissertation is an individual work, I could have never accomplished this without their help.

I am also grateful to thank Dr. Reza Zoughi, Dr. Jie Huang, Dr. Xiaoming He, Dr. David Pommerenke, and Dr. Rosa Zheng for serving on my committee and their valuable guidance.

I would also like to thank all my dear teachers, colleagues, and friends in Applied Microwave Nondestructive Testing Laboratory (*amntl*).

Last but not least, I am grateful with all of my being to my family, for everything they gave me during my life. I believe I never could have embarked on my Ph.D. journey and finished it without an overwhelming support from my lovely mother and father.

The work was supported in part by the US Department of Defense STTR Phase II project W31P4Q-16-C-002.

TABLE OF CONTENTS

Page

SECTION

PAPER

SECTION

LIST OF ILLUSTRATIONS

Page

PAPER I

PAPER II

PAPER III

LIST OF TABLES

Page

PAPER I

NOMENCLATURE

Symbol	Description
β	Bistatic Angle
λ	wavelength
f	frequency
ε	dielecric properties
ε_r	relative (to free-space) dielectric constant
μ	permeability
k	wavenumber
SNR	signal-to-noise ratio
d	baseline length
Z	range

1. INTRODUCTION

1.1. MILLIMETER WAVE IMAGING SYSTEM

Microwave and millimeter wave imaging methods, based on synthetic aperture radar (SAR) algorithms, are capable of producing three-dimensional (3D) holographic images of dielectric structures. Such imaging methods have been extensively used for nondestructive testing (NDT) and are becoming widespread in their utility. More specifically, SAR imaging is particularly valuable for inspecting the ever-increasing composite structures that are replacing metals in many industries [1]-[4]. Additionally, SAR imaging has utility in biomedical, security, geophysics and remote sensing applications [5], [6].

Millimeter wave imaging is based on collecting the coherent backscattered fields from an illuminated object (target). To reconstruct an object's image, the backscattered field should be collected over a known two-dimensional (2D) plane by a 2D array of antennas (probes) called imaging aperture plane. This collection can be achieved by a single antenna which mechanically scans the object over the 2D plane. The advantage of this technique (raster scan with a single antenna) is the high quality reconstructed image due to adequate spatial sampling which meet Nyquist Criteria. Moreover, utilizing a single antenna for scanning minimizes the interference issue caused by mutual coupling between array elements. However, the bottleneck of this technique is the large time requirement to complete the scan and therefore this type of imaging system cannot be used for real-time imaging. To speed-up the imaging process, a one- or two-dimensional (1D/2D) array of antennas can be used [7]-[8]. For instance, in imaging systems designed by Pacific

Northwest National Laboratory (PNNL) [8], a 1D array which is mechanically scanned is utilized to produce a 2D image. To further reduce scan time, a 2D array can be used to electronically scan and collect the backscattered field in two directions rapidly.

Real-time imaging systems have been used for many applications as discussed in [7]. In many applications such as those of [9]-[11], high cross-range resolution (i.e., the ability to distinguish two adjacent targets) is required. Near the imaging aperture, the resolution is dependent on the sampling density of the aperture (i.e., distance between the array elements which also dictates the array element size). However, at larger distances, in particular when the distance is large with respect to the array aperture size, the image resolution becomes a function of the array aperture size and the resolution degrades rapidly with distance (as dictated by the physics of wave propagation) [2]. However, enlarging the array aperture size to reach high resolution is challenging due to requirements of a tightly spaced measurement grid (half wavelength spacing of working frequency) dictated by Nyquist criteria for aliasing-free image reconstruction. Hence, to achieve an aliasing-free high resolution imaging system, a large dense array is required, which leads to increased complexity and cost of the imaging system.

Generally, 2D array imaging systems can operate in a monostatic or bistatic mode. In monostatic mode, the same antenna is used for transmitting and receiving signals. Monostatic imaging configuration suffers from limited dynamic range due to difficulties in isolating the receiver hardware from the transmitter signals. Moreover, these difficulties increase for the very large frequency bandwidth required for 3D imaging. The limited isolation leads to signals directly coupling from the transmitter to the receiver, which are mainly due to limited directivity or aperture reflections in the antenna. These signals saturate the receiver which subsequently result in a reduction of the overall dynamic range, thereby limiting the measurement system. On the other hand, bistatic configurations provide a relatively large dynamic range due to the high isolation between the receiver and transmitter circuitry. This improved isolation is achieved by using two separate antennas. Also, since the transmitter and receiver are located separately, a bistatic configuration has the ability to distinguish targets from clutter [12]. Hence, many investigations have focused on the development of efficient SAR algorithms for bistatic imaging configurations [13]-[14]. There are numerous imaging algorithms such as Time-domain Back Projection [14], Polar Formation Algorithm [14], and Non-Linear Chirp Scaling Algorithm [12] that can be used for SAR imaging. All of these algorithms are fundamentally implemented for monostatic configuration, but can be used for a bistatic (or quasi-monostatic) configuration. However, most of these algorithms cannot properly produce the image for a bistatic configuration, leading to image distortion [14]. This problem is caused by the dependency of these bistatic imaging algorithms to the transmitter-receiver geometry. A bistatic configuration can be approximated as a monostatic configuration (i.e., a quasi-monostatic configuration). This was achieved by translating the raw data obtained from a bistatic configuration to an equivalent monostatic model. However, using this equivalent model introduces image distortion since this model is an approximation, hence quantifying image distortion caused by this approximation is needed.

1.2. RESEARCH OBJECTIVE

The goal of this dissertation is to design, prototype and test an innovative millimeter wave imaging system that operates in the frequency range of 33-35 GHz and is capable of producing rapid images of various diverse scenes. To reduce the cost of the imaging system as discussed in [15], multiplexing array elements is suggested. In this method, instead of using individual transceivers for each array element, the signal received by the array elements is routed to a single transceiver by RF switches. The high isolation provided by the switching network allows such systems to produce images with fidelity comparable to that of scanning with a single detector, while the electronic switching allows for real-time and video frame-rate imaging speeds. The major drawback of physical arrays is the difficulty in providing densely sampled apertures due to physical size and cost restrictions. The antenna (array element) size limits the number of antennas that can be used in the array, and a large array with a relatively smaller number of elements (large sparse array) generates aliasing in the images. In this work (similar to [16] and [17]), to reduce aliasing, a non-uniform distribution of antennas is utilized for the array of the imaging system. However, as shown in [18], there is no practical statistical or optimization technique that can be used to arrive at an optimum non-uniformly spaced array element distribution. Hence, based on the work in [18], a random distribution is used for array element's placement.

As it relates to SAR image processing and as discussed in Section 1.1, most of the image reconstruction algorithms are implemented for monostatic imaging configurations. However, the bistatic configuration, which is highly desired, is utilized in imaging systems due to the ability of providing large dynamic range. To this end, a bistatic configuration can be approximated as a monostatic configuration (*i.e.*, a quasi-monostatic configuration). Here, the ω-k SAR algorithm as a fast and efficient algorithm that is optimized for monostatic configuration ([2] and [19] paper) can be used to generate 3D images from bistatic measurements. Similar to [14], the bistatic processing was performed by the less complex monostatic algorithm. This was achieved by translating the raw data obtained from a bistatic configuration to an equivalent monostatic model. This equivalent monostatic model consists of a transceiver antenna (*i.e.*, the transmitter and receiver are collocated), which is located in the middle of the distance between the bistatic transmitter and receiver configuration (Tx/Rx pair). Utilizing this equivalent model introduces image distortion due to phase differences between the roundtrip monostatic range and bistatic range. In this work, the image distortion that results from using an equivalent monostatic model for bistatic measurements in SAR imaging was investigated for both far and near field imaging. Moreover, conditions for negligible image distortion are studied for bistatic imaging systems with different layouts of transmitter/receiver (Tx/Rx) pairs in an imaging system. In addition, to suppress error in reconstructed image caused by phase differences between equivalent monostatic model and bistatic configuration, phase compensation method is proposed and applied to different layouts of Tx/Rx pairs.

Finally, a comprehensive form of the range migration algorithm (RMA) is analytically derived for reconstructing the reflectivity function (image) in imaging systems. More specifically, amplitude compensation, in addition to the typical phase compensation, is included in the development of the matched filter of the RMA, and is herein referred to as the amplitude compensated RMA (AC-RMA). The proposed algorithm is robust that can successfully reconstruct the reflectivity function of a target with high resolution regardless of its dielectric contrast, including scenarios with low contrast between the dielectric properties of the background and target in the presence of noise. This approach is also independent of the bandwidth of the imaging system and is applicable to multilayer media. Moreover, the efficacy of the proposed AC-RMA does not degrade when the backscattered signal is received by monostatic or bistatic configurations.

1.3. ORGANIZATION OF THE DISSERTATION

The design of the proposed imaging system requires investigating and developing millimeter wave hardware and imaging algorithms. This dissertation focuses on improving the hardware design in Paper I, investigating image distortion in paper II, and developing an improved imaging algorithm in paper III.

In PAPER I, titled “A Sparse Ka-band SAR 1D Imaging Array using an Asymmetric Antipodal Vivaldi Antenna”, a sparse array with an optimum number of Tx/Rx pairs (minimum number of pairs without disturbing image quality) is designed to reach a large aperture size. To this end, a two-layer antipodal Vivaldi antenna operating in the 35 to 40 GHz frequency range is designed and optimized for high gain and reduced squint in the radiation pattern as compared with conventional antipodal Vivaldi antenna designs [20]. The improved compact antipodal Vivaldi antenna is implemented as the element in two 8-element switched (1D) sub-arrays for making Tx/Rx pairs inimaging system. Each element (antenna) is located with random spacing between adjacent antennas in both sub-arrays. The 1D non-uniform switched sub-arrays were fabricated and used for SAR imaging purposes. The resulting images by the proposed array proves that the proposed 1D non-uniform sub-array provides sufficient signal level and bandwidth to scan a target comprehensively with a factor of four reduction in scanning time compared with imaging using a single Tx/Rx pair to reach real-time imaging speeds.

PAPER II, titled “Image Distortion Characterization due to Equivalent Monostatic Approximation in Near Field Bistatic SAR Imaging”, investigates the distortion level in the images produced using bistatic configuration in both far and near field imaging. As discussed in Section 1.2, the monostatic model is preferred for its computational efficiency, while bistatic measurements are preferred for their sensitivity. Hence, due to the simplicity of the equivalent monostatic model, it is desirable to extend the monostatic model to bistatic imaging. However, translating the raw data obtained from a bistatic configuration to an equivalent monostatic model causes image distortion that needs to be quantified. In [12] and [14], conditions were proposed for the negligible image distortion in far field imaging. Here, the root-mean-square (RMS) error is used to quantify the image distortion and negligible image distortion are determined for bistatic imaging systems with different layouts of transmitter/receiver (Tx/Rx) pairs. Moreover, a phase compensation method is proposed and applied for bistatic imaging systems with different layouts of Tx/Rx pairs to minimize image distortion when equivalent monostatic model is employed.

In PAPER III, titled “A Comprehensive Bi-Static Amplitude Compensated Range Migration Algorithm (AC-RMA)”, a comprehensive algorithm is developed, to reach reconstructed image with high quality (minimum image distortion). AC-RMA can successfully reconstruct the reflectivity function (image) of a target with high quality regardless of its dielectric property, including scenarios with low contrast between the dielectric properties of the background and target in the presence of noise. Moreover, reconstructed image quality by the AC-RMA is independent on transmitter and receiver’s layouts of imaging system in particular, sparse non-uniform imaging system.

PAPER

I. A SPARSE KA-BAND SAR 1D IMAGING ARRAY USING AN ASYMMETRIC ANTIPODAL VIVALDI ANTENNA

ABSTRACT

This paper presents an improved antipodal Vivaldi antenna for millimeter wave imaging applications (frequency range of 35 to 40 GHz). Opposed to a (traditional) balanced antipodal Vivaldi antenna design, the new design is optimized for small dimensions using only two layers. Also, the E-plane beam tilt (i.e., the off-axis pattern squint) is substantially reduced as compared to conventional Vivaldi antennas. Lastly, unwanted radiation in the side and back lobes of the new antenna is reduced due to improved matching. An optimized corrugated ground plane, asymmetric exponential radiated arms and tapered slot edges (TSE) are used in the new structure. These design improvements were made with the goal of integrating it into imaging arrays where reducing antenna size, increasing the bandwidth, and reducing back and side lobes is important. The performance of the antenna when used for wideband SAR imaging was first tested using raster scanning. Subsequently, this antenna was integrated into a compact and sparsely sampled one-dimensional (1D) array for real-time synthetic aperture radar (SAR) imaging applications. The 1D array is designed as two non-uniformly spaced transmitter and receiver sub-arrays in order to reduce aliasing in the images. The performance of this 1D array is demonstrated with imaging multiple targets.

1. INTRODUCTION

Microwave and millimeter wave imaging using synthetic aperture radar (SAR) techniques is capable of producing high resolution images for many critical applications related to security, medical imaging and nondestructive testing [1-4]. To produce a high resolution image, the backscattered signals from a target are collected by raster scanning over a known one- or two-dimensional (1D or 2D) grid [3]. For this, raster scanning can be performed using a single antenna (monostatic mode) or two antennas (bistatic mode). Typically antennas with wide beamwidth are particularly desired for high resolution SAR imaging in the synthetic array near-field [5]. However, as raster scanning is time consuming and requires bulky electromechanical hardware, the raster scanning can be realized electrically through the implementation of monostatic or bistatic antenna arrays similar to the microwave imaging camera in [1], [3], [4], [6] and [7]. Typically, the array element spacing is chosen to be less than or equal to one quarter and one half of the operating wavelength for monostatic and bistatic arrays, respectively [8]. This spacing limitation keeps the sampling rate higher than or equal to the Nyquist criterion (in order to obtain alias-free images) and therefore obtain high resolution images. Hence, a compact and small antenna is desirable in order to satisfy the Nyquist criterion. Moreover, it is beneficial to use wide band antennas in the imaging array to improve image range resolution [9]. To this end, many efforts have investigated the design of compact wideband antennas such as [6], [7] and [10]. In addition, it is desirable that these antennas directly integrate with other parts of the system such as switches in order to facilitate a compact imaging system. As such, printed circuit board (PCB) based antennas are often desired for this application [9], [11]. Furthermore, end-fire radiation is desired for PCB-based antennas used for imaging applications in order to facilitate placement of the antennas (within the array) on the edge of the PCB with minimal radiated energy to other parts of the imaging system. To this end, a compromise is made between wide beamwidth of the antenna for high resolution imaging and increased directivity for reducing interference between array elements when designing SAR-based imaging arrays. As such, a small PCB-based Vivaldi tapered slot antenna with its planar structure, directive radiation pattern, and relatively wide beamwidth is chosen as the element of choice for imaging arrays [11].

There are three main types of PCB-based Vivaldi tapered slot antennas: coplanar, antipodal, and balanced antipodal, all of which are illustrated in Figure 1 [12]. One main difference between these three types is related to their feed transition, which can be implemented via microstrip, strip line, grounded co-planar waveguide (GCPW), or substrate integrated waveguide (SIW). The antenna in Figure 1 (a), suffers from limited bandwidth and distorted radiation pattern due to surface current perturbation in the transition [13]. On the other hand, the antipodal Vivaldi antenna (Figure 1 (b)) has relatively wider bandwidth compared to the coplanar design [12]. However, this antenna has a slight tilt in the polarization direction, and high side lobe level (SLL) and squint in the radiation pattern (beam-tilting in the E-plane). For imaging purposes, a tilt in the polarization direction may not necessarily be a limitation, however the beam tilt and the high SLL can lead to increased interference between array elements. Thus, to reduce polarization tilt and squint, a balanced antipodal configuration (See Figure 1 (c)) with a stripline feed is suggested in [12]. However, fabrication of this multilayer structure, especially at microwave and millimeter wave frequencies, is relatively more complex than one based on a two-layer PCB design.

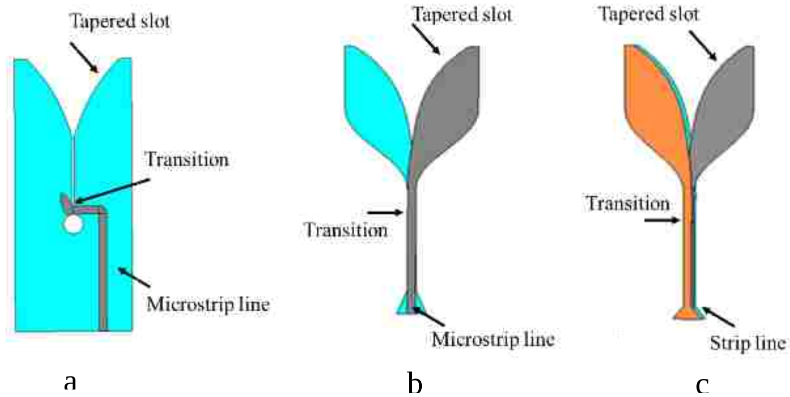

Figure 1. Vivaldi antenna designs: (a) tapered slot (coplanar), (b) antipodal, and (c) balanced antipodal.

In this work, an improved compact antipodal Vivaldi antenna is designed, operating in the frequency range of 35 to 40 GHz, which does not produce radiation pattern squint and high SLL. The designed antenna is used as the building block in a sparse 1D (linear) imaging array for producing high resolution SAR images. This antenna is designed on a two-layer PCB for ease of fabrication, but unlike the balanced antipodal configuration, the design employs modifications in the transition between the feed line and the antenna to reduce unwanted radiation and pattern squint. In Section 2, the antenna design optimization using CST Microwave studio® is presented. In Section 3, the properties of the antenna were experimentally measured and compared with simulation. Additionally, a pair of antennas was used along with raster scanning to test their efficacy for imaging. Subsequently, in Section 4, 16 of the designed antennas were assembled in a 1D transmitter/receiver array pair (8 elements each for the transmitter and receiver sub-arrays) in which each element routes the signal to the transmitter/receiver via microwave switches (multiplexers). SAR images resulting from bistatic scanning using this 1D array are provided and the imaging results illustrate the utility of this design for use in imaging systems.

2. ANTENNA DESIGN AND SIMULATION

The new implementation of an antipodal Vivaldi antenna with a GPCW feed and tapered slot edges (TSE) for SLL reduction that operates from 35 to 40 GHz is illustrated in Figure 2. A GCPW is utilized as the feed line in order to better confine the electric field, as compared to a microstrip feed line, as well as to interface directly with other components of the imaging array such as RFICs [6]. Corrugations are included in the transition (as shown) and optimized along with the curvature profile of the taper, indicated as f(y), to improve the matching and radiation pattern. The dimensions and curvature profile of both arms of the antenna are optimized to obtain minimum squint in the radiation pattern for this two layer design (without adding an extra layer). Additionally, the corrugation improves coupling of the electric field between the two arms of the antenna, providing a better match from the feed line to the radiating end. This reduces unwanted radiation from the transition which improves radiation efficiency and reduces pattern squint. Simulations were performed to optimize the antenna parameters for operation at the desired frequency range. The antenna is designed on a 10 mils-thick Rogers 4350B substrate, with the optimized dimensions shown in Table I. Detailed descriptions of the effect of each design feature on the antenna radiation properties is provided below.

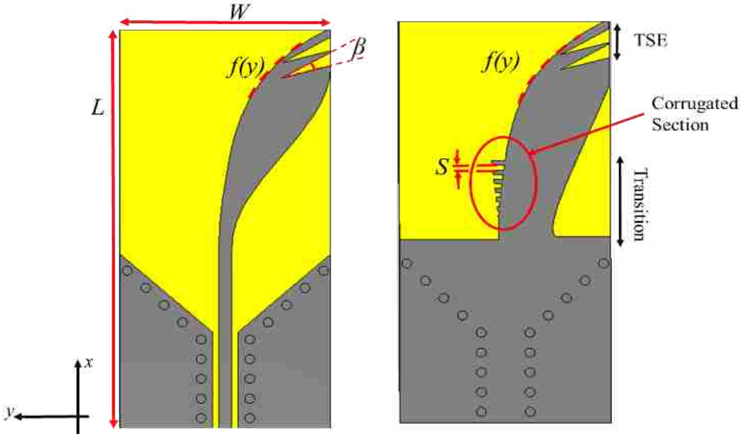

a b

Figure 2. The new antipodal Vivaldi antenna: (a) top layer, (b) bottom layer.

Table 1. Antipodal Vivaldi antenna dimensions.

Parameters	Dimensions
W	6.5 mm
L	13.2 mm
β	14.6°
S	0.15 mm

Initially the designed antenna was optimized in order to improve matching (i.e., reduce the reflection $|S_{11}|$) between the corrugated metalized arm in the bottom layer and the top layer’s metalized arm. More specifically, for a design threshold of -10 dB or lower from 35 to 40 GHz, the curvature profile, *f(y)*, which is illustrated in Figure 2 and defined in (1), was optimized.

$$f(y) = c_1 e^{Ry} + c_2 \tag{1}$$

In (1), the exponent term, R (defined as the opening rate), along with coefficients c1 and c2, are optimized independently (via simulation) for the top and bottom arms in order to minimize $|S_{11}|$. As shown in Figure 3, using different curvature profiles for the top and bottom arms produces better matching than using the same profile for both. The optimized coefficients for the bottom arm profile are $R = 0.65$, $c_1 = 0.5$, and $c_2 = 0.2$, and for the top arm are $R = 0.55$, $c_1 = 0.95$, and $c_2 = 0.2$. This asymmetric configuration also improves the pattern squint issue as will be shown later. The results in Figure 3 show that the asymmetric configuration provides an $|S_{11}|$ of less than -10 dB over the full operating frequency range. Moreover, this asymmetric design provides more bandwidth with a lower $|S_{11}|$ than the conventional symmetric designs. Another feature that was implemented in this design was tapered slot edges (TSE) at the outer edge of the metalized arm to suppress SLLs and increase gain (similar to [14]). As mentioned in [14], the outer edge of the antenna arms plays an important role in the antenna’s radiation pattern and consequently, the gain, by reducing the intensity of the outer edge currents.

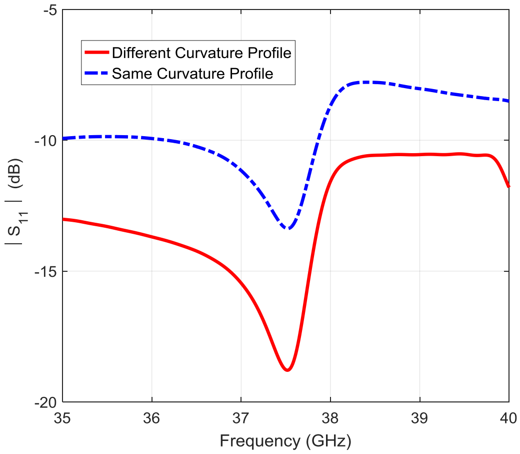

Figure 3. $|S_{11}|$ of the new antenna with the same and different curvature profiles.

As mentioned in [14], the outer edge of the antenna arms plays an important role in the antenna's radiation pattern and consequently, the gain, by reducing the intensity of the outer edge currents. In other words, reducing outer edge currents and directing them toward the opening exponential curve of the tapered slot in the antipodal configuration increases the directivity (and gain) without enlarging the antenna [14]. In addition, as discussed in [14], besides the improvement in SLL, the squint effect is reduced by optimizing the TSE. The TSE angle β (value shown in Table 1) is optimized via simulation and the gain of the antenna with and without TSE is depicted in Figure 4. As shown, the gain of the antenna with TSE is greater than that of the same antenna without TSE for the full operating frequency range.

Next, to increase electric field density between the arms and thus reducing leakage and improving matching, corrugations in the form of five thin stubs were included in the new design, as illustrated in Figure 2.

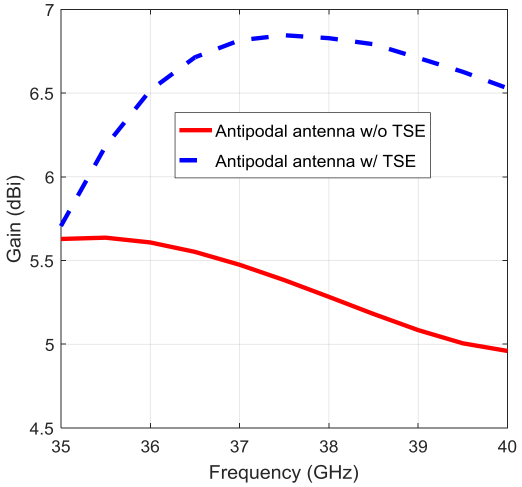

Figure 4. Antenna gain with and without TSE.

Next, to increase electric field density between the arms and thus reducing leakage and improving matching, corrugations in the form of five thin stubs were included in the new design, as illustrated in Figure 2. The length of these stubs changes linearly from 0.08 mm to 0.4 mm in order to provide gradually increased coupling between the top arm and the bottom arm within the taper section only. The interval between the corrugations, S, was optimized using simulation in order to concentrate the majority of the electric field at the ends of the antenna and subsequently reduce SLLs. To this end, the effect of corrugations and their interval (*S*) on the E-plane directivity at 38 GHz (near the upper end of operating frequency range, which is more affected by the corrugation interval) is shown in Figure 5. As seen, in the absence of corrugations, the antenna's main lobe directivity is less than the case with corrugations. Moreover, SLL of the antenna without corrugations is higher, in particular around 180° (antenna's back lobe). For *S* = 0.15 mm or higher, minimum SLLs are obtained; specifically, the improvements are the back-lobe and the sides at around 125°

and 250°. Based on [15], the corrugation interval must be kept lower than 1/6 of the resonance frequency's wavelength-where radiation from the corrugations is negligible. In this design, for corrugation intervals of 0.15 mm or larger, the antenna's E-plane directivity is essentially equivalent to that when *S* = 0.15 mm. Hence, in this work, corrugations with *S* = 0.15 mm is selected for the overall lowest SLL.

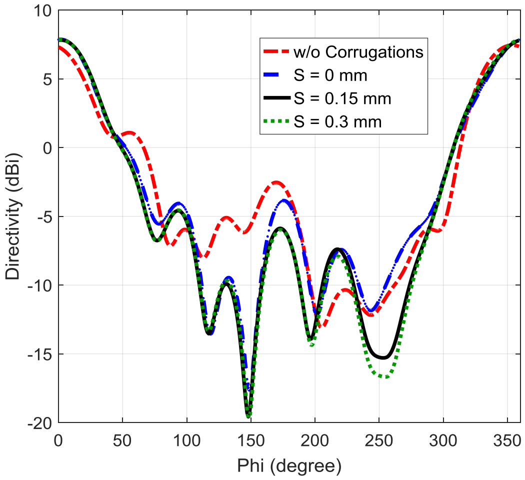

Figure 5. Antenna directivity for different corrugation intervals at 38 GHz.

The combination of these design features results in a reduction of surface current perturbations in the transition as a result of improved control of the transition impedance [15]. By controlling the transition's impedance, a majority of the electric field remains contained between the feed line and ground plane in the transition, rather than as unwanted radiation due to surface current perturbation. The overall improvements in the antenna properties due to these features can also be demonstrated through the radiation pattern of the antenna. To this end, the directivity at 35 GHz for Theta = 90° (E-plane) is shown in Figure 6 (a) for the proposed antenna with optimized dimensions and compared to a conventional design (Figure 1 (b)) in order to demonstrate the improvement provided by this new design. As seen, the conventional antenna has a 15° squint from the antenna center (at Phi = 345°). This improvement is attributed to utilizing the TSE as discussed in [14] and the corrugated ground plane that improves electric field coupling between the antenna arms. Also, the maximum SLL in the proposed design is approximately 5 dB lower than the conventional antipodal antenna. This reduction in SLL in the new design is the result of improved matching in this asymmetric design. In addition, directivity patterns of both the proposed and conventional antennas for Phi = 0° (H-plane) are depicted in Figure 6 (b). As seen, the proposed antenna has wider beam width in the H-plane as compared with the conventional one. Such a feature is desired for SAR imaging to obtain maximum overlapped coverage when using separate transmitter and receiver antennas (i.e., a bistatic imaging configuration). Moreover, the back lobe level of the designed antenna is 10 dB less than that of the conventional antenna. This is advantageous as it relates to minimizing interference between the antenna and other parts of the imaging system, namely, the millimeter wave circuitry.

3. ANTENNA MEASUREMENT RESULTS

3.1. ANTENNA PROPERTY MEASUREMENT

In order to support the improvements illustrated above via simulation, two antenna were fabricated with the dimensions given above in Table I. To begin, the reflection coefficient ($|S_{11}|$) of the designed antenna was measured, as is shown in Figure 7 along with the simulated results.

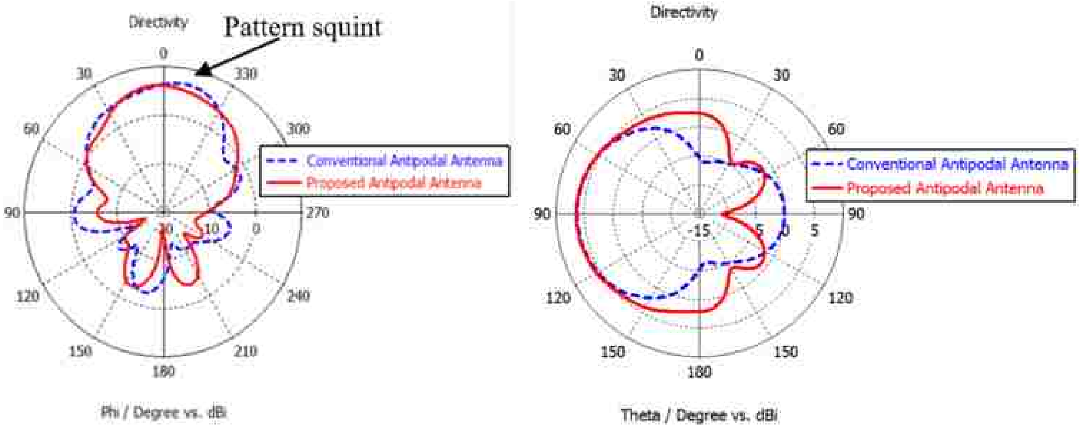

a

b

Figure 6. Directivity of the new and conventional antenna at 35 GHz in the (a) Theta = 90° (E-plane) and (b) Phi = 0° (H-plane).

Both simulated and measured results have acceptable matching ($|S_{11}| \leq -10$ dB) and exhibit resonance at around 37.6 GHz (mid-frequency of the antenna's bandwidth). In addition, the gain of the antenna was measured by connecting the two antennas to two ports of a calibrated Anritsu MS4644A VNA. In this way, one antenna serves as transmitter and one as receiver, and the transmission coefficient (S_{21}) was measured for four sets of specified separation distances (between 20 mm or 2.5λ at the center frequency and 60 mm or 7.5λ at the center frequency). Then, using the Friis transmission equation, the gain was calculated from each S_{21} measurement [18]. The average measured gain, from all separation distances, is shown in Figure 8 along with simulated results for comparison. As seen, there is good agreement between simulation and measurement results, both of which show a gain greater than 5.7 dBi throughout the operating frequency range. The ripple that is evident in the measured gain is attributed to multiple reflections (the effect of which was not fully removed by averaging the set of measurements).

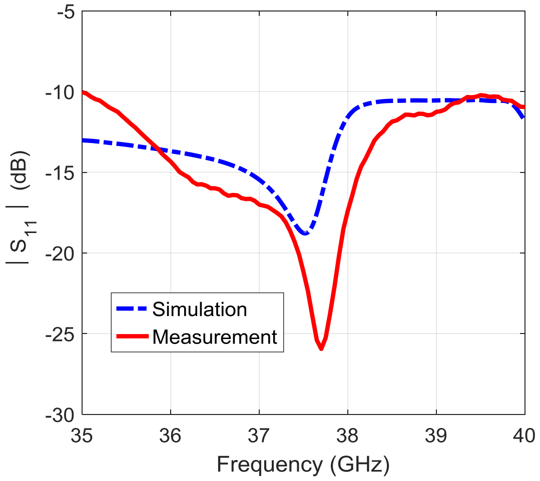

Figure 7. Simulated and measured $|S_{11}|$ of the new antenna.

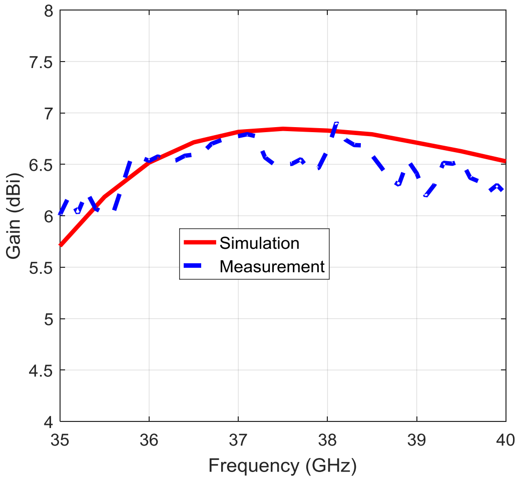

Figure 8. Simulated and measured gain of the new antenna.

3.2. SAR IMAGING USING TWO ANTENNAS

Now, to demonstrate the efficacy of the designed antenna for imaging applications, two experiments were performed in the frequency range of 35 to 40 GHz. The experimental set up is depicted in Figure 9. For these experiments, the two fabricated antennas were mounted above a scan table side by side (14 mm center to center distance between the antennas), with 40 mm standoff distance between the antennas and the scan table (i.e., the target range). The antennas were connected to two ports of a calibrated Anritsu MS4644A VNA. The antenna connected to Port 1 of the VNA was used as the transmitter, and the antenna connected to Port 2 served as the receiver (i.e., a bistatic configuration). For each experiment, a target was placed on the scan table and moved in a two-dimensional raster pattern with a uniform 2 mm spacing grid in both dimensions. The amplitude and phase of the transmission coefficient, S21, was measured and subsequently used for SAR image processing by utilizing the equivalent monostatic model in [19]. Here, for the first experiment, a 4 mm diameter metallic ball (shown in Figure 10 (a)), placed on a low density foam, with dielectric properties similar to air, was imaged, as shown in Figure 10 (b). For the second experiment a target consisting of four parallel aluminum strips approximately 40 mm long and 4 mm wide, and spaced by 20, 10, and 5 mm as well as one cross-shaped aluminum patch with dimensions of 50 mm x 5 mm for each leg were placed on the foam substrate, as shown in Figure 10 (c). The resultant SAR image is shown in Figure 10 (d). The image of the metallic ball is clear (red circle) without additional noise. Similarly, a low noise and high contrast image is obtained for the second target, except for ghost indications between the two upper parallel strips in the image of the second target. These are the result of the interaction between these closely spaced strips and the direction of wave polarization being perpendicular to the strips. These results show the efficacy of these antennas for wideband and high resolution SAR imaging due to the large bandwidth, high radiation efficiency (appropriate gain and directivity) and low unwanted radiation from the sides and back of the new design.

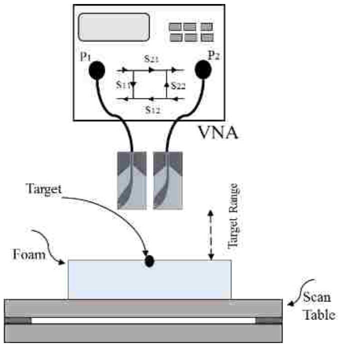

Figure 9. Measurement setup for scanning target.

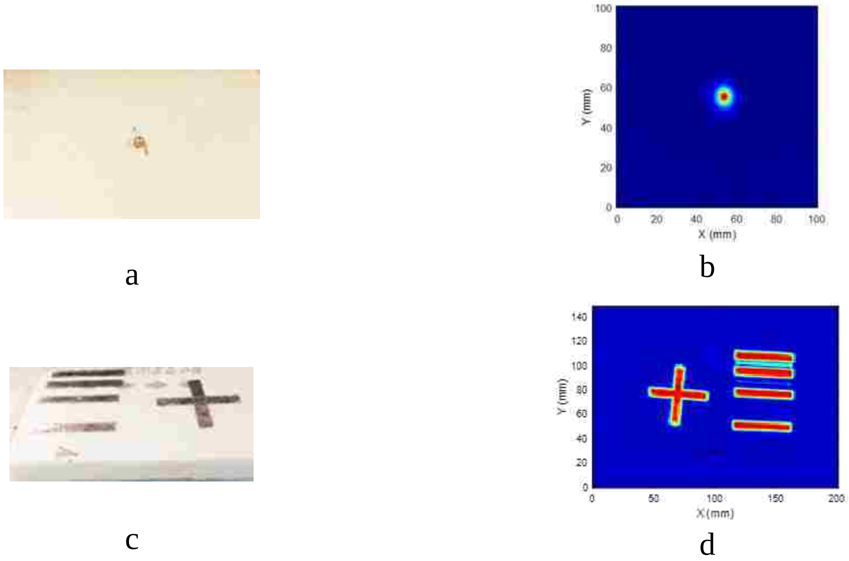
a
b
c
d

Figure 10. (a) Photograph of metallic ball target, (b) magnitude of SAR image of metallic ball, (c) photograph of aluminum strips and cross target, and (d) magnitude of SAR image of aluminum strips and cross target.

4. IMAGING ARRAY

4.1. ARRAY DESIGN

As mentioned in Section I, imaging systems based on 1D or 2D antenna arrays can be used instead of raster scanning for real-time imaging. Also, as mentioned in [6], for far field imaging, the cross-range resolution can be enhanced at large distances from the array by increasing the array aperture size. However, an appropriately sampled (with λ/4 spacing to meet Nyquist criterion) large array will require a large number of array elements which leads to increased complexity and cost. A large array with a relatively smaller number of elements can be realized by increasing the baseline length (distance between transmitter and receiver antenna) of transmitter/receiver element pairs at the expense of generating aliasing in the images. These conditions are defined based on visible image distortion as explained in [19]. Therefore, to reduce aliasing for a large array with a relatively small number of elements, non-uniform baseline length between elements can be used (similar to [5] and [20]). However, as shown in [21], there is no practical statistical or optimization technique that can be used to arrive at an optimum non-uniformly spaced array element distribution. In this work, based on the work in [21], random baseline length is used for all elements based on equal probability (non-biased selection). With such a non-uniformly-spaced array, a SAR image can be constructed using an approach similar to the non-uniform imaging method of [5] using a minimum number of measurements. To this end, the new antenna is implemented as the element in two 8-element switched (1D) sub-arrays for the transmitter and receiver, respectively. Each element (antenna) was located with random spacing between adjacent antennas in both sub-arrays, with the schematic of the element placement shown in Figure 11. For both transmitter and receiver sub-arrays, four ADRF5020 switches and two Wilkinson power combiner/dividers were used to connect each antenna to amplifiers (HMC635LC4 as the driver amplifier in the transmitter sub-array and HMC1040LP3CE as the low noise amplifier in the receiver array). These amplifiers were used to compensate for losses due to the switches and PCB. The switch losses, for a frequency range of 30-40 GHz (beyond the specified range of recommended frequency range of the components) were measured to be 4 dB at 30 GHz and remained constant for most of the band, and then sharply increases to 8 dB at 36 GHz. The PCB losses are approximately 2 dB/inch, and the Wilkinson divider in each port contributes and additional (measured) 4 dB of loss. In this way, the signal loss from the measurement port (connector) to each antenna in the array is approximately 22 to 25 dB within the desired bandwidth. The amplifiers gain compensates for a majority of this loss. The fabricated transmitter and receiver random sub-arrays are shown in Figure 12 (a) and (b), respectively. In Figure 12 (c), the controller board for controlling switches and supplying power to both arrays is shown. These two sub-arrays were stacked with distances of 10 mm, resulting in the measurement pattern shown in Figure 11.

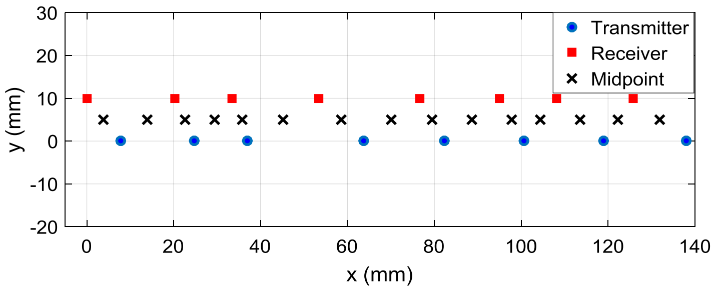

Figure 11. The relative locations of the elements in the non-uniformly spaced transmitter and receiver sub-arrays.

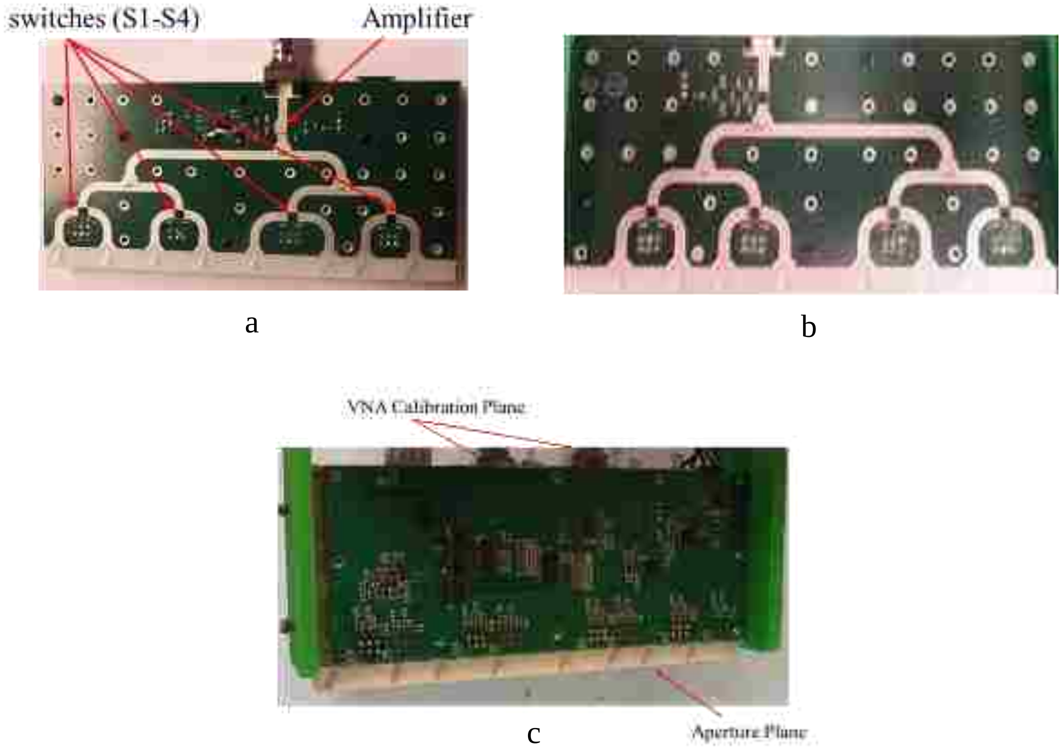

Figure 12. Sub-array board with switches, Wilkinson power combiner/dividers and (a) HMC635LC4 amplifier for transmitter and (b) HMC1040LP3CE amplifier for receiver. (c) Controller board, which is attached to a holder.

4.2. IMAGING RESULTS

Imaging experiments were conducted using the assembled 1D imaging array, connected to two ports of a calibrated VNA as above, and a raster scanner. A measurement pattern was used where the transmitters and receivers were sequentially operated in adjacent pair combinations to perform bistatic measurements. This resulted in fifteen measurements using fifteen adjacent transmitter/receiver pairs as indicated by the midpoint markers in Figure 11. This measurement pattern produced a minimum sampling distance of 11.3 mm, a maximum distance of 19.5 mm and an average spatial sampling of 14.4 mm along the x-axis. This average spacing value is larger than one wavelength in this frequency range and therefore can cause severe aliasing. To reduce aliasing in the reconstructed images, the array can be shifted along x direction to obtain additional measurements or signal processing techniques such as compressed sensing and spectral estimation techniques can be used [22-23].

The target image is constructed using the measured S21 and the monostatic SAR algorithm [5]. As shown in [18], the equivalent monostatic model can be used for each bistatic pair of the array and the middle point of each pair's baseline length is chosen as the equivalent transceiver location. To apply SAR to the measured S21, a common phase reference (reference plane) is required which is set at the aperture plane of the array (Figure 12c), while the reference plane for the measured S21 is defined per the VNA calibration plane (at the end of the cable). Hence, the reference plane must be shifted from VNA calibration plane to the aperture plane for all frequencies. To do this, additional measurements are required before scanning targets. To this end, first, the transmitter and receiver sub-arrays were connected to ports 1 and 2 of the VNA, respectively. Then, in order to remove the static reflections from sub-arrays and surrounding structures, the backscattered signal from the base foam was measured in the absence of the target and coherently subtracted from the measured backscattered signal prior to SAR processing. In addition, to remove the effect of phase changes due to switches, amplifiers and traces, the calibration method of [9] using transmission through measurements with an identical antenna was applied.

The array was placed along the x direction and scanner was used to move the sample linearly (in the y direction with steps of 2 mm) beneath the array. The array provided fifteen equivalent monostatic spatial measurement points across its length (across the x-axis) and was scanned along the y-axis with a step size of 2 mm. As discussed before, this spatial sampling provided by the array is large and causes image aliasing. To reduce aliasing, the array was shifted along x-axis two times with 3 mm step to collect 45 overall spatial measurement points across the array length (along the x-axis) for each y location. SAR images of two targets (a metallic ball and aluminum strip and cross patch) were obtained using this array from a distance of 45 mm and shown in Figure 13. As shown, the image shows a clear indication of the scanned targets, though not with the same quality of a raster scanned single pair of antennas (see Figure 10). The reduced image quality is mainly due to calibration error (especially error in the phase calibration of the arrays used to set the exact reference plane) causing variation among the array elements. Despite this lower image quality, the resulting image proves that this compact design, using the new antipodal Vivaldi antenna and minimum number of switches provides for a sufficient signal level and bandwidth to scan the target comprehensively using 8-element transmitter and receiver sub-arrays, resulting in a factor of four reduction in scanning time. The scan time can be further reduced if using a dedicated and faster sweeping transceiver instead of the general purpose VNA.

Finally, the array was used to scan targets from larger distances. To this end, three 10 mm × 10 mm (< λ of working frequencies) metallic square patches located on foam background were used as a target (Figure 14(a)). The transmitter and receiver sub-arrays scanned the target two times, one time for a 90 mm (~ 10λ) target range and other for 145 mm (~ 15λ). As shown in Figure 14 (b), the target dimensions are precisely addressed in the reconstructed image for a range of 90 mm.

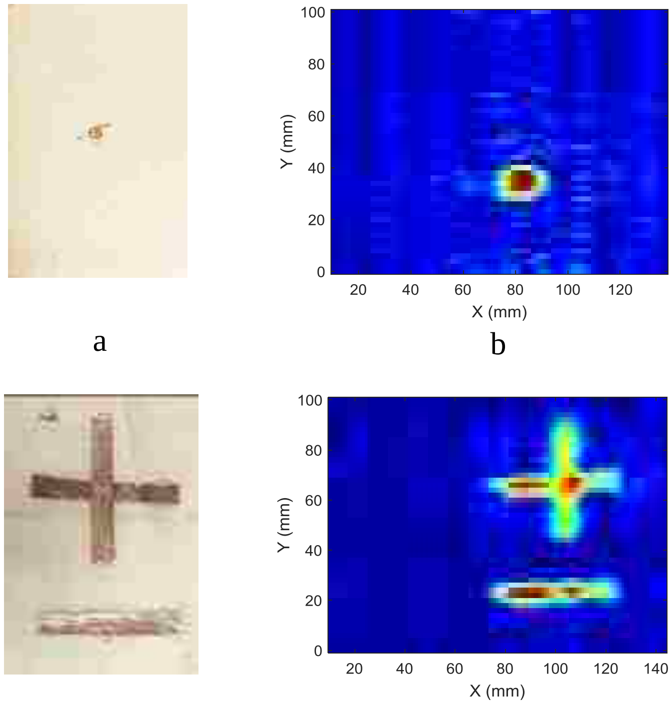

a b

c d

Figure 13. (a) Photographic and (b) SAR image of the metal ball target. (c) Photographic and (d) SAR image of the aluminum strip and cross patch with transmitter/receiver array.

The transmitter and receiver sub-arrays scanned the target two times, one time for a 90 mm (~ 10λ) target range and other for 145 mm (~ 15λ). As shown in Figure 14 (b), the target dimensions are precisely addressed in the reconstructed image for a range of 90 mm. However, for larger distances (around the sub-array's aperture size), beside ghost indications around the reconstructed image of the target, the target dimensions are not equal to those of the target (see Figure 14 (c)). This is mainly due to reduced signal to noise ratio (SNR) at this larger distance. In this case, as discussed in [19], noise power becomes the dominant parameter that affect reconstructed image quality when using the equivalent monostatic model approximation for SAR processing.

5. CONCLUSION

In this work, a two-layer antenna antipodal Vivaldi antenna in Ka-band is designed and optimized. As discussed, the asymmetric structure and corrugated shape of ground plane are the core modifications for solving the squint and matching problems in a wide bandwidth antipodal Vivaldi antenna. These modifications results in the two layers of the antipodal Vivaldi antenna having similar properties (back lobe level less than -20 dB and squint angle equals 0°), similar to the multilayer balanced antipodal Vivaldi antenna in [24], but with less fabrication complexity. The modification also results in increased electric field coupling between arms, and as such, the squint of the radiation pattern decreases. Beside these core modifications, TSE is utilized on the top and bottom layer metalized arms in order to increase the antenna's gain and reduce SLLs. Hence, the designed antenna is sufficient for use in imaging systems due to its low unwanted radiation and proper gain with compact size. To this end, this compact, low weight and relatively high gain antenna was utilized as an array element for SAR imaging applications. More specifically, a 1D non-uniform switched array, employing this antenna as the array element, was fabricated and used for imaging. In the designed non-uniform array, the baseline length of transmitter/receiver pairs varies between one and two wavelengths of the mid-band frequency. In the feed line, a switch was used to access each array element individually and amplifiers were utilized to enhance SNR and compensate for losses caused by the switch and power splitters as well as in the traces on the PCB. This 1D array was used to provide electronic scanning in one dimension while it was moved in the other dimension to generate 2D SAR images with up a scan time improvement of a factor of 4.

The obtained SAR images of the targets considered had high image resolution with minor image quality degradation (as compared to a single raster scanned result). Overall, this design can be extended to a 2D array for real-time imaging without the need for raster scanning.

REFERENCES

M. T. Ghasr, S. Kharkovsky, R. Bohnert, B. Hirst, R. Zoughi, "30 GHz linear high-resolution and rapid millimeter wave imaging system for NDE", *IEEE Trans. Antennas Propag.*, vol. 61, no. 9, pp. 4733-4740, Sep. 2013.

M. Azghani, P. Kosmas, F. Marvasti, "Microwave medical imaging based on sparsity and an iterative method with adaptive thresholding", *IEEE Trans. Med. Imag.*, vol. 34, no. 2, pp. 357-365, Feb. 2015.

D. M. Sheen, D. L. McMakin and T. E. Hall, "Three-dimensional millimeter-wave imaging for concealed weapon detection," in IEEE Transactions on Microwave Theory and Techniques, vol. 49, no. 9, pp. 1581-1592, Sept. 2001.

S. S. Ahmed, A. Schiessl and L. Schmidt, "A Novel Fully Electronic Active Real-Time Imager Based on a Planar Multistatic Sparse Array," in *IEEE Transactions on Microwave Theory and Techniques*, vol. 59, no. 12, pp. 3567-3576, Dec. 2011.

J. T. Case, M. T. Ghasr, R. Zoughi, "Optimum 2-D nonuniform spatial sampling for microwave SAR-based NDE imaging systems", IEEE Trans. Instrum. Meas., vol. 61, no. 11, pp. 3072-3083, Nov. 2012.

M. T. Ghasr, M. J. Horst, M. R. Dvorsky, R. Zoughi, "Wideband microwave camera for real-time 3-D imaging", *IEEE Trans. Antennas Propag.*, vol. 65, no. 1, pp. 258-268, Jan. 2017.

M. T. Ghasr, M. A. Abou-Khousa, S. Kharkovsky, R. Zoughi and D. Pommerenke, "Portable Real-Time Microwave Camera at 24 GHz," in IEEE Transactions on Antennas and Propagation, vol. 60, no. 2, pp. 1114-1125, Feb. 2012.

J. Paden, "Bistatic/monostatic synthetic aperture radar for ice sheet measurements" in Electrical engineering and computer science, University of Kansas, 1999.

M. A. Baumgartner, M. T. Ghasr, R. Zoughi, "Wideband imaging array using orthogonally fed dual varactor-loaded elliptical slots", *IEEE Trans. Instrum. Meas*., vol. 64, no. 3, pp. 740-749, Mar. 2015.

M. A. Abou-Khousa, M. T. Ghasr, S. Kharkovsky, D. Pommerenke and R. Zoughi, "Modulated Elliptical Slot Antenna for Electric Field Mapping and Microwave Imaging," in IEEE Transactions on Antennas and Propagation, vol. 59, no. 3, pp. 733-741, March 2011.

J. Bai, S. Shi and D. W. Prather, "Modified Compact Antipodal Vivaldi Antenna for 4–50-GHz UWB Application," in IEEE Transactions on Microwave Theory and Techniques, vol. 59, no. 4, pp. 1051-1057, April 2011.

Y. S. Amrullah, K. Paramayudha and Y. Wahyu, "Enhancement performance tapered slot vivaldi antenna for weather radar application," *2016 International Seminar on Intelligent Technology and Its Applications (ISITIA)*, Lombok, pp. 329-332, 2016.

J. Bai, S. Shi, D. W. Prather, "Modified compact antipodal vivaldi antenna for 4–50-GHz UWB application", *IEEE Trans. Microw. Theory Tech*., vol. 59, no. 4, pp. 1051-1057, Apr. 2011.

A. De Oliveira, M. Perotoni, S. Kofuji, J. Justo, "A palm tree antipodal Vivaldi antenna with exponential slot edge for improved radiation pattern", *IEEE Antennas Wireless Propag*., vol. 14, pp. 1334-1337, 2015.

H. Galal, M. Agio, “High efficient light extraction and directional emission from large refractive-index materials with a planar Yagi-Uda antenna,” Opt. Mater. Express 7, 1634–1646, 2017.

M. El Gibari, D. Averty, C. Lupi, YMH Li, S. Toutain, "Coplanar-Microstrip Transitions for Ultra-Wideband Communications.", *Ultra wideband communications: novel trends-antennas and propagation*. ISBN 978-953-307-452-8, INTECH, 2011.

T. M. Weller, L. P. B. Katehi, G. M. Rebeiz, H. J. Cheng, J. F. Whitaker, "Fabrication and characterization of microshield circuits", *Int. Symp. Space Terahertz Technol.*, 1993-Mar.

J. A. Shaw, "Radiometry and the Friis transmission equation", *Amer. J. Phys*., vol. 81, no. 1, pp. 33-34, Jan. 2013.

Z. Manzoor, M. T. Ghasr, K. M. Donnell. "Image distortion characterization due to equivalent monostatic approximation in near field bistatic SAR imaging." *Instrumentation and Measurement Technology Conference (I2MTC), 2017 IEEE International*, pp. 1-5. IEEE, 2017.

L. Wang, A. M. Al-Jumaily, R. Simpkin, "Investigation of antenna array configurations using far-field holographic microwave imaging technique", Progress In Electromagnetics Research M, vol. 42, pp. 1-11, 2015.

Y. T. Lo, "A mathematical theory of antenna arrays with randomly spaced elements", *IEEE Trans. Antennas Propag.*, vol. AP-12, no. 3, pp. 257-268, May 1964.

X. Yang, Y. R. Zheng, M. T. Ghasr and K. M. Donnell, "Microwave Imaging From Sparse Measurements for Near-Field Synthetic Aperture Radar," in IEEE Transactions on Instrumentation and Measurement, vol. 66, no. 10, pp. 2680-2692, Oct. 2017.

J. T. Case, M. T. Ghasr and R. Zoughi, "Nonuniform Manual Scanning for Rapid Microwave Nondestructive Evaluation Imaging," in IEEE Transactions on Instrumentation and Measurement, vol. 62, no. 5, pp. 1250-1258, May 2013.

N. Wang, M. Fang, H. Chou, J. Qi and L. Xiao, "Balanced Antipodal Vivaldi Antenna With Asymmetric Substrate Cutout and Dual-Scale Slotted Edges for Ultrawideband Operation at Millimeter-Wave Frequencies," in IEEE Transactions on Antennas and Propagation, vol. 66, no. 7, pp. 3724-3729, July 2018.

II. IMAGE DISTORTION CHARACTERIZATION DUE TO EQUIVALENT MONOSTATIC APPROXIMATION IN NEAR FIELD BISTATIC SAR IMAGING

ABSTRACT

The ω-k synthetic aperture radar (SAR) algorithm is a computationally efficient algorithm for near field three-dimensional (3D) monostatic SAR imaging in nondestructive testing applications. However, bistatic measurements are preferred in order to obtain high dynamic range, in particular when real-time imaging arrays are used. This paper investigates the image distortion caused by using an equivalent monostatic imaging algorithm for bistatic measurements. Simulation and measurements at millimeter wave frequencies in Ka-band (26.5 – 40 GHz) are used to investigate the resultant image distortion. Further, the image distortion is quantified through root-mean-square (RMS) error which is calculated as a function of bistatic transmitter-receiver separation distance, range and noise power. Simulations and measurements are conducted for imaging using raster scanning of a pair of antennas and for non-uniform imaging arrays. Additionally, an approximate method for phase compensation is introduced to improve image error from the monostatic approximation of bistatic measurement.

1. INTRODUCTION

Microwave and millimeter wave imaging methods, based on synthetic aperture radar (SAR) algorithms, are capable of producing three-dimensional (3D) holographic images of dielectric structures. Such imaging methods have been extensively used for nondestructive testing (NDT) and are becoming widespread in their utility. More specifically, SAR imaging is particularly valuable for inspecting the ever-increasing composite structures that are replacing metals in many industries [1]- [4]. Additionally, SAR imaging has utility in biomedical, security, geophysics and remote sensing applications [5], [6]. As it relates to SAR image processing, the ω-k SAR algorithm is a fast and efficient algorithm that is optimized for monostatic (i.e., the transmitting and receiving antennas are collocated) SAR imaging [7], [8]. However, measuring instruments for monostatic imaging configurations may suffer from limited dynamic range due to difficulties in isolating the receiver hardware from the transmitter signals. Moreover, these difficulties increase for the very large frequency bandwidth required for 3D imaging. The limited isolation leads to signals directly coupling from the transmitter to the receiver, which are mainly due to limited directivity or aperture reflections in the antenna. These signals saturate the receiver which subsequently result in a reduction in the overall dynamic range, thereby limiting the measurement system.

Bistatic configurations provide a relatively large dynamic range due to the high isolation between the receiver and transmitter circuitry. This improved isolation is achieved by using two separate antennas. Also, since the transmitter and receiver are located separately, a bistatic configuration has the ability to distinguish targets from clutter [9]. Hence many investigations have focused on the development of efficient SAR algorithms for bistatic imaging configurations [10]- [12].

There are numerous imaging algorithms such as Time-domain Back Projection [12], Polar Formation Algorithm [12], and Non-Linear Chirp Scaling Algorithm [9] that can be used for SAR imaging. All of these algorithms are fundamentally implemented for monostatic configuration, but can be used for a bistatic (or quasi-monostatic) configuration. However, most of these algorithms cannot properly estimate the image for a bistatic configuration, leading to image distortion [12]. This problem is caused by the dependency of these bistatic imaging algorithms to the transmitter-receiver geometry. A bistatic configuration can be approximated as a monostatic configuration (i.e., a quasi-monostatic configuration). Therefore, a fast and efficient FFT-based monostatic imaging algorithm such as the ω-k SAR algorithm can be used to generate 3D images from bistatic measurements. In [12] and [13], the bistatic processing was performed by a (less complex) monostatic algorithm. This was achieved by translating the raw data obtained from a bistatic configuration to an equivalent monostatic model. This equivalent monostatic model consists of a transceiver antenna (i.e., the transmitter and receiver are collocated), which is located in the middle of the distance between the bistatic transmitter and receiver configuration as shown in Figure 1. Using this equivalent model introduces image distortion since this model is an approximation. This approximation can be valid (i.e., little distortion) when the ratio of range (target distance from the transmitter/receiver plane) and baseline length (i.e., distance between the transmitter and receiver) is large and thus the monostatic range becomes equal to the bistatic range. However, when the target is near the synthetic aperture plane, this approximation creates image distortion since the bistatic range becomes larger than the monostatic range, as is illustrated in Figure 1.

In [9] and [12], conditions were proposed to make the image distortion negligible. Specifically, a very short baseline length (d) in comparison with range (RR and RT) is a prime condition that was considered in [9] and [12]. This condition was defined to obtain negligible distortion in the produced images by the equivalent monostatic model. In [9], the proposed condition is that the baseline length is less than half of the wavelength of the transmitted signal. In [12], the proposed condition is that the difference between the bistatic range and the monostatic range must be less than a quarter-wavelength to produce negligible image distortion. Overall, these conditions were applicable for far field imaging where the range is much larger than the baseline length. However, in near field imaging, the conditions proposed by [9] and [12] may not always apply since the range can be on the order of the baseline length. In this work, the definition of the boundary between near field and far field imaging for a bistatic configuration is different from that of the traditional antenna definition and considered in [9] and [12]. That is to say, the boundary is defined based on the phase difference between the roundtrip monostatic range, 2R, and bistatic range, RR + RT. With respect to the bistatic configuration, the near field is defined as the region where this phase difference is not negligible. This phase difference, which corresponds to an image error threshold of -10 dB will be shown later.

Due to the simplicity of the equivalent monostatic model, it is desirable to extend the monostatic model to bistatic near field imaging. To this end, this paper (as an extension of [13]), investigates the distortion level in the images produced using bistatic measurements that are processed with the simple and fast monostatic ω-k SAR algorithm. The root-mean-square (RMS) error is used to quantify the image distortion. Simulations were performed in order to calculate this RMS error as a function of bistatic baseline length, range and noise level. Based on the RMS error results, conditions are recommended for bistatic configurations to produce negligible image distortion (low RMS error). Pertinent measurements are performed to validate the simulation results.

Finally, conditions for negligible image distortion are determined for bistatic imaging systems with different layouts of transmitter/receiver (Tx/Rx) pairs. Different layouts have been studied in many works such as [7] and [14] in order to increase the aperture size and subsequently the image resolution of the imaging system. In addition, it is desirable to minimize the number of Tx/Rx pairs utilized in the system to reduce complexity and cost of the imaging system. To this end, one Tx/Rx pair can be chosen to raster scan on a one or two-dimensional (1D or 2D) grid uniformly or non-uniformly, as suggested in [7]. However, this solution is very time consuming. Thus, to reduce the time requirement, a uniform or non-uniform 1D or 2D array consisting of Tx/Rx pairs can be used (similar to [14-16]). Further, to enlarge the aperture of the imaging system using the minimum number of Tx/Rx pairs, a sparse non-uniform array is suggested in [17]. In all of these cases, the layout and number of Tx/Rx pairs in the system have an important effect on image distortion. Hence, here, the RMS error of the reconstructed image is calculated when the bistatic baseline length of the Tx/Rx pairs is equal for all pairs (uniform sampling) and when Tx/Rx pairs have different baseline length (non-uniform sampling). From this, conditions for negligible image distortion are determined as it relates to the number and layout of Tx/Rx pairs. Moreover, because the phase differences between bistatic measurement and monostatic model is the primary factor that causes image distortion, a phase compensation method is proposed in Section V to minimize this difference. Simulation and measurement are provided to show the efficacy of the phase compensation method on reducing image distortion.

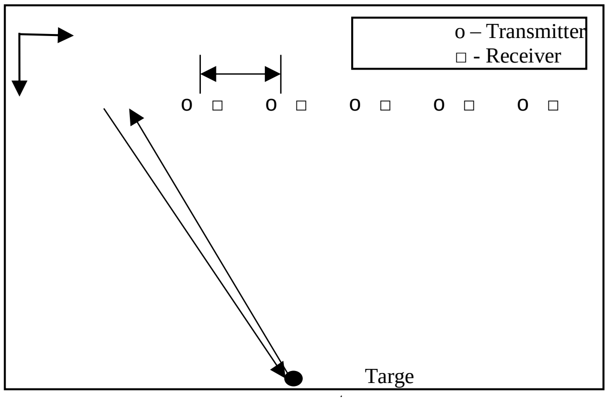

a

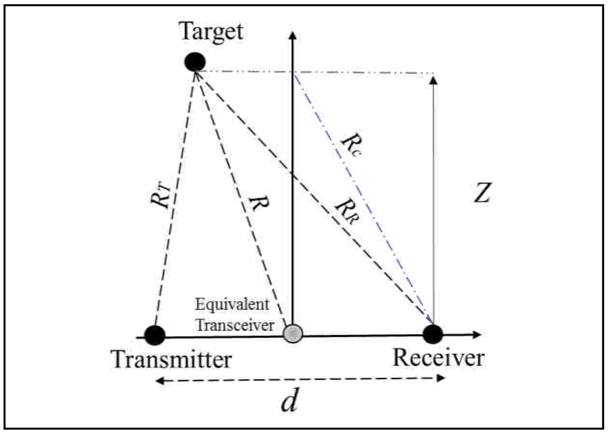

b

Figure 1. (a) Schematic of a bistatic 1D scan for imaging a target, and (b) bistatic configuration with defined baseline range and bistatic angle.

2. BISTATIC GEOMETRY AND SIMULATION RESULTS

In general, near field SAR imaging is performed by raster scanning a wideband transceiver on a one- or two-dimensional (1D or 2D) grid. The investigation in this Section only considers a 1D line scan, as shown in Figure 1. In this Figure, a simplified schematic is shown where a transceiver (transmitter and receiver in a bistatic configuration) is scanned across a 1D path with a step size of Δx, thereby synthesizing a wideband linear array (Figure 1a). This 1D synthetic array is used to create a SAR image of the target. As the interrogating signal propagates from the transmitter to the target and back to the receiver, it undergoes a phase change of $e^{-jk(R_T+R_R)}$, where R_T and R_R are defined in Figure 1. However, using an equivalent monostatic SAR model, the image is created by compensating for $e^{-jk(2R)}$ of phase change (typically performed in the Fourier domain). When the baseline length (d) is much smaller than the range R (*i.e.,* small bistatic angle, $\beta = \arctan(d/2Z)$, as defined in [18]), $R_T + R_R$ better approximates $2R$, and therefore it is expected that the image distortion will be low. On the other hand, when the bistatic angle becomes large, such as when operating in the near field of the array (i.e., small R), the image distortion is expected to increase. This image distortion is quantified as an RMS error (E), as shown in (1) and discussed in [7]:

$$E = \sqrt{\frac{\sum_x \sum_y \sum_z \left(\left| I_m(x,y,z) \right| - \left| I_b(x,y,z) \right| \right)^2}{\sum_x \sum_y \sum_z \left(\left| I_m(x,y,z) \right| \right)^2}} \tag{1}$$

Simulations were performed at Ka-band (26.5 – 40 GHz) to illustrate this error. More specifically, the simulated synthetic array had a length of 200 mm and was sampled at $\Delta x = 2$ mm ($\Delta x < \lambda/4$ at mid-band frequency) [2]. For the simulations, point sources were considered for the synthetic array elements, and a point scatterer was used as the target. The simulations were performed for a baseline length of $d = 10$ mm to $d = 20$ mm (approximately corresponding to $\lambda < d < 2\lambda$ at mid-band frequency), and a range of $Z = 20$ mm to 200 mm (approximately corresponding to $2\lambda < Z < 20\lambda$). In addition, additive white

Gaussian noise was added to the simulated data. Initially, the noise power was set to -150 dB (i.e., ideal situation with no noise), simulating close to ideal conditions. The noise power was defined as an absolute power level since the signal level reduces with range (resulting from attenuation due to free-space wave propagation). This specific noise level is low for the simulated range, Z, and was not the primary contributor to image distortion (i.e., ideal measurements). For each array and target configuration, an image, I_b, was calculated. Also, for each range distance, Z, the reference image, I_m, was calculated using a monostatic configuration (i.e. $d = 0$). Figure 2(a) shows an example simulated reference image for a point target located at $Z = 100$ mm, and the corresponding bistatic image for a baseline length of $d = 14$ mm is shown in Figure 2(b). The images in Figure 2 show that a bistatic configuration distorts the point target image primarily in the form of a widened indication. The RMS error, E (in dB), for the simulated results is shown in Figure 3. This figure shows that when baseline length (d) is small, the image error is independent of range (Z). However, for large values of d, which can be greater than the wavelength of the transmitted signal, the error reduces with distance. Typically, image distortion resulting from an error less than -10 dB is not readily visible and thus $E = -10$ dB can be considered the threshold for obtaining a low distortion image. By considering this threshold for acceptable image distortion and based on the simulated results in Figure 3, it can be concluded that negligible image distortion can be obtained when 2β is less than 10° (corresponding to $Z/d > 6$), even for large d ($\geq \lambda$), as seen in Figure 3. This region also corresponds to the far field region with respect to the bistatic baseline length as explained above.

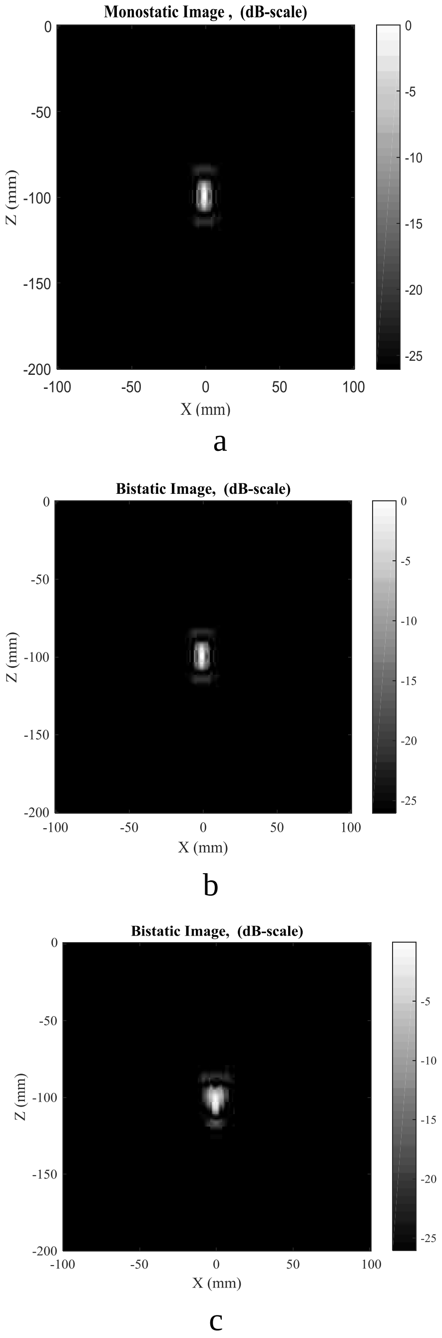

Figure 2. (a) SAR image of a point target using a monostatic approach, and SAR image of a point target using a bistatic configuration with (b) d = 14 mm and (c) d = 50 mm.

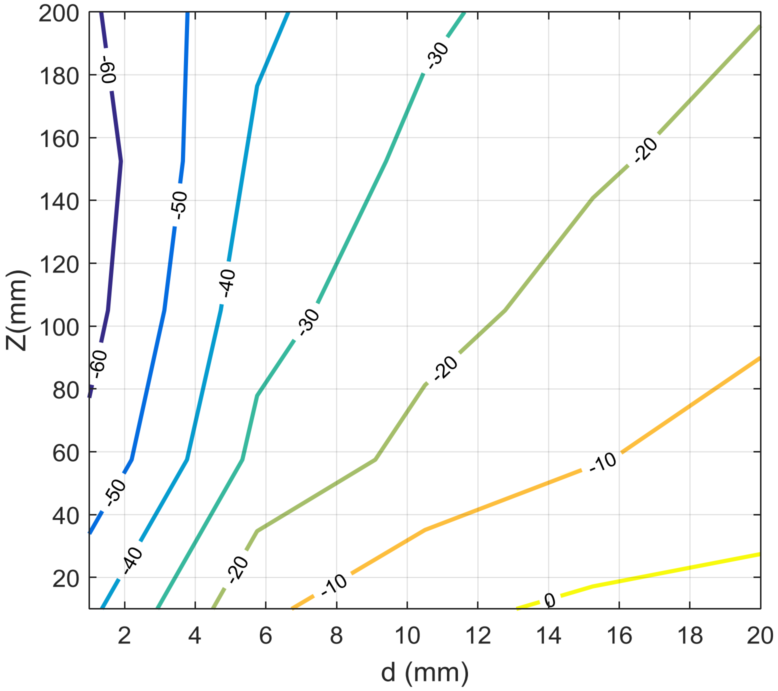

Figure 3. *E* contours (dB scale) as a function of range (*Z*) and baseline length (*d*) for a 200 mm long Ka-band synthetic array and additive noise power of -150 dB.

These simulations were repeated for an additive noise power of -75 dB. This noise level was chosen to correspond to the dynamic range of commercial vector network analyzer at millimeter wave frequencies such as Ka-band which accounts for all noise sources of the measuring instrument. In practice, there exist no other major sources of noise at the frequency range considered here (26.5 – 40 GHz) since the VNA is a tuned receiver and other signals in the environment, which are not common at these frequencies, are filtered out. Furthermore, additional sources of noise which can be due to clutter (other reflections) from the environment can be minimized in the measurements and thus not included in the simulations. The error contour results are shown in Figure 4. This figure shows that in the presence of realistic noise levels, the image distortion is primarily due to the presence of noise for large values of *Z*. For example, as shown in Figure 4, *E* is equal to -5 dB for targets located at 180 mm, regardless of the baseline length (*d*). Figure 5 shows *E* contours as a function of noise power and baseline length, *d*. This figure shows that noise power is the primary contributor to *E* when *d* is small, and that *d* is the primary contributor to *E* when noise is low (*e.g.*, lower than -70 dB).

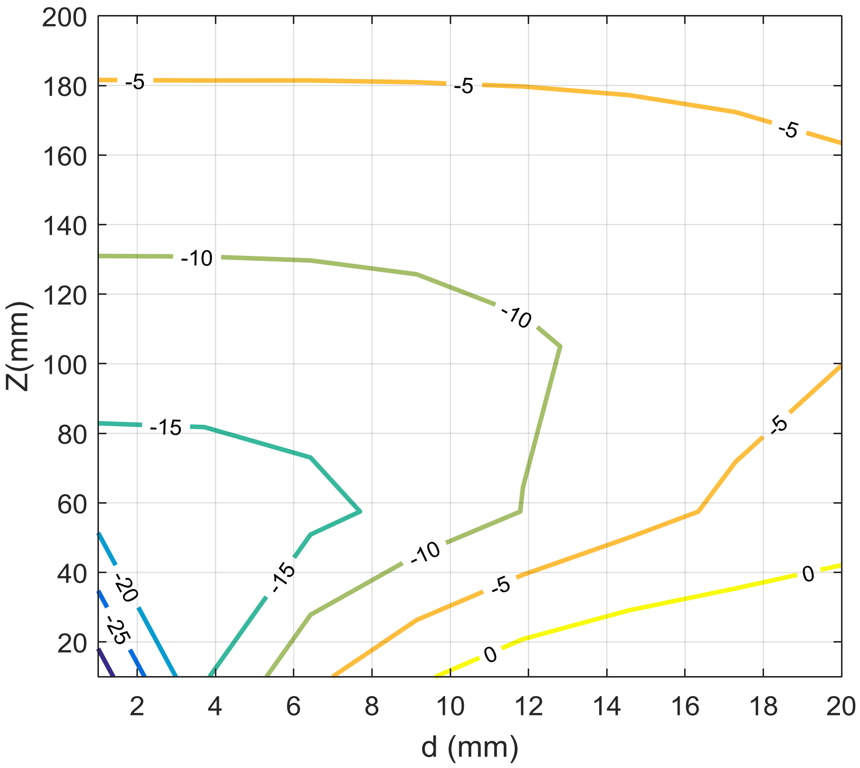

Figure 4. *E* contours (dB scale) as a function of range (*Z*) and baseline length (*d*) for a 200 mm long Ka-band synthetic array and additive noise power of -75 dB.

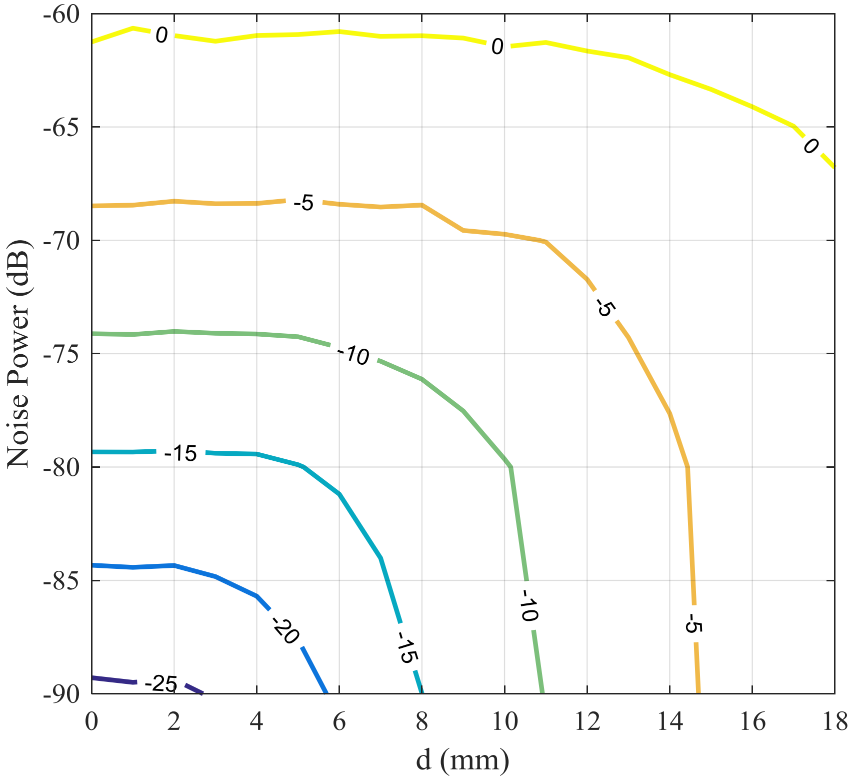

Figure 5. *E* contours in terms of noise power and baseline length (*d*) for range *Z* = 40 mm.

Next, image distortion in the near field region is discussed, where phase differences between roundtrip monostatic range and bistatic range cannot be ignored. Non-negligible phase differences in bistatic configuration is the result of large bistatic angle. To study image error as a function of bistatic angle, with respect to β definition, *E* in terms of *d* (normalized to λ) is depicted in Figure 6 for different *Z/d*. As shown, for *Z/d* > 6 (corresponding to $2\beta < 10°$), image distortion is just dependent on *Z/d* even for large value of *d* (≥ λ). On the other side, for *Z/d* < 6 (near field), *d*/λ is a critical factor in image distortion and for *d* > λ, error is more than -10 dB.

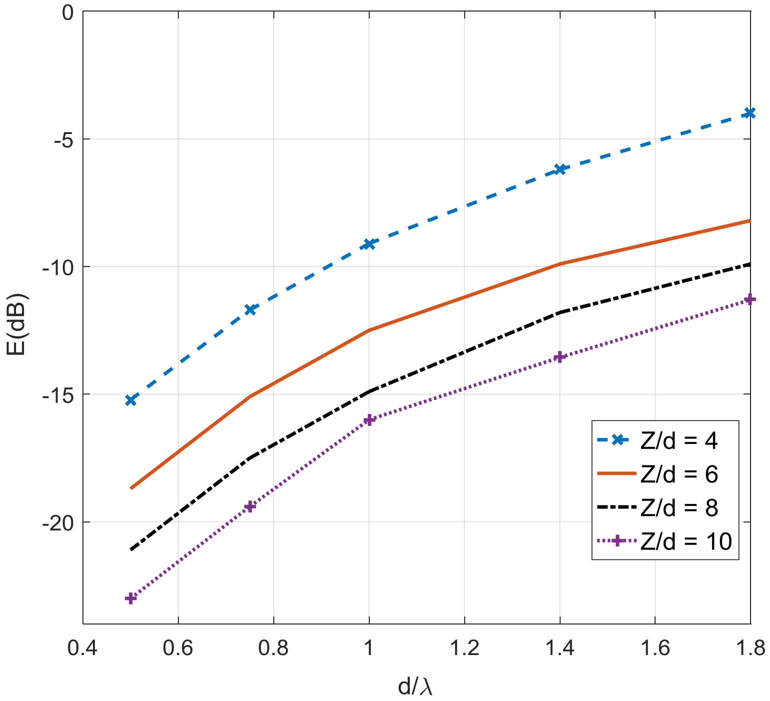

Figure 6. *E* contours in terms of *d* (normalized to λ) for different *Z/d*.

3. MEASUREMENT RESULTS

To experimentally validate the simulation results, the setup in Figure 7 was used. Two WR-28 (Ka-band) waveguides were connected to two calibrated ports of an Anritsu MS4644A VNA and used as transmitter and receiver antennas. S_{11} (reflection coefficient at port 1) is used to obtain the reference monostatic image and S_{21} was used to create the bistatic image. A metallic ball (diameter of 4 mm) was used as the target point scatterer which was held on a foam platform (to represent free space). By considering 50 mm × 50 mm aperture plane, the target was linearly scanned with a 2 mm step size and various baseline length values. Figure 8 shows the measured and simulated *E* as a function of baseline length for a range equal to 45 mm. The measured results of the near field measurement shown are the average of 5 measurements at each baseline length (*d*). Several simulations were performed at various noise power levels (-76 dB to -70 dB to represent expected noise levels from the measurement setup) as shown in Figure 8. The measurement results followed the simulation results except for when the baseline length was large (*i.e.*, a bistatic angle greater than 10 degrees). The differences between measurement and simulation can be attributed to the fact that the target is not a point scatterer, as the diameter of the target (4 mm) is on the order of a half-wavelength (λ/2) in the frequency range used (λ/2 at the mid-band frequency is around 4.5 mm). More importantly, the waveguide antennas are also not point sources (as assumed in simulation), and therefore for a large baseline length, the directivity of the waveguide antennas (compared to point sources) will further influence the received signal. Additional scattering from the scanner may also contribute to the image distortion.

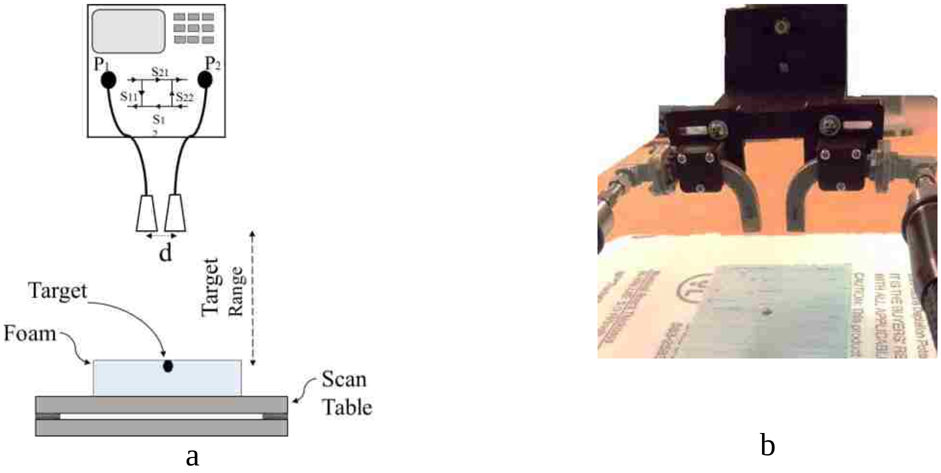

Figure 7. Measurement (a) schematic and (b) setup.

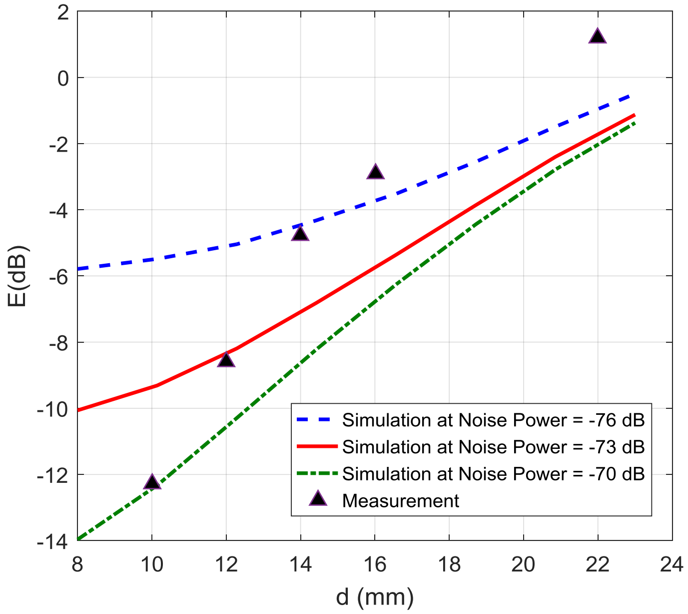

Figure 8. Measured and simulated *E* in terms of baseline length at *Z* = 45 mm.

4. SAR IMAGES BY IMAGING SYSTEMS WITH DIFFERENT BISTATIC LAYOUTS

In this section, image distortion of the equivalent monostatic model for a bistatic configuration is studied for 3 different Layouts of Tx/Rx pairs, as illustrated in Figure 9. Specifically, in Layout 1 (Figure 9(a)), one Tx/Rx pair with a fixed baseline length, *d*, scans the target uniformly with a sampling step of 2 mm in both the *x* and *y* directions ($\Delta x = \Delta y = 2$ mm). Layout 2 (Figure 9(b)), illustrates a 1D imaging array of Tx/Rx pairs with non-uniform spacing (oriented in the *x*-direction) that is typically used to reduce imaging time (instead of 2D raster scanning). This array is used to scan the target in the *y* direction with $\Delta y = 2$ mm to form a 2D image. Here, *d* of each Tx/Rx pair in the array is chosen randomly (uniform random distribution spaced between minimum and maximum baseline lengths of one and two wavelengths, respectively), while the number of Tx/Rx pairs and Δy are chosen based on the number of sampling points necessary to achieve minimum image distortion as discussed in [7] and derived in this paper. Layout 3, shown in Figure 9(c), depicts a fixed non-uniformly spaced 2D imaging array.

First, to find the required number of Tx/Rx pairs (number of sampling points), E contours (dB scale) as a function of Z and sampling points numbers (N) is shown in Figure 10 for Layouts 2 and 3. In these simulations, a point target is scanned by using a 200 mm × 200 mm aperture plane. Here, the range variation of d (maximum and minimum d) is chosen based on a fixed number of sampling points and a given aperture size. Figure 10(a) shows the contour plot of the image error (E) as a function of the number of sampling points and range, Z.

For example, to obtain $E < -10$ dB for $Z = 40$ mm, a minimum of 4000 sampling points are required. However, as Z increases, a smaller number of points becomes necessary. Since for Layout 2, the scan is uniform in the y-direction with $\Delta y = 2$ (101 points in y-direction), the required 4000 points translates to ~40 Tx/Rx pairs in the non-uniform 1D array used in the x-direction. Figure 10(b) shows the E contours when using Layout 3 for imaging the same target with the same aperture size as Figure 10(a). As shown, the image error, E, is generally independent of Z. Therefore, to achieve $E < -10$ dB, more than 50 Tx/Rx pairs are required. To this end, in this work, 40 and 55 Tx/Rx pairs are chosen for the rest of the simulations of Layouts 2 and 3, respectively.

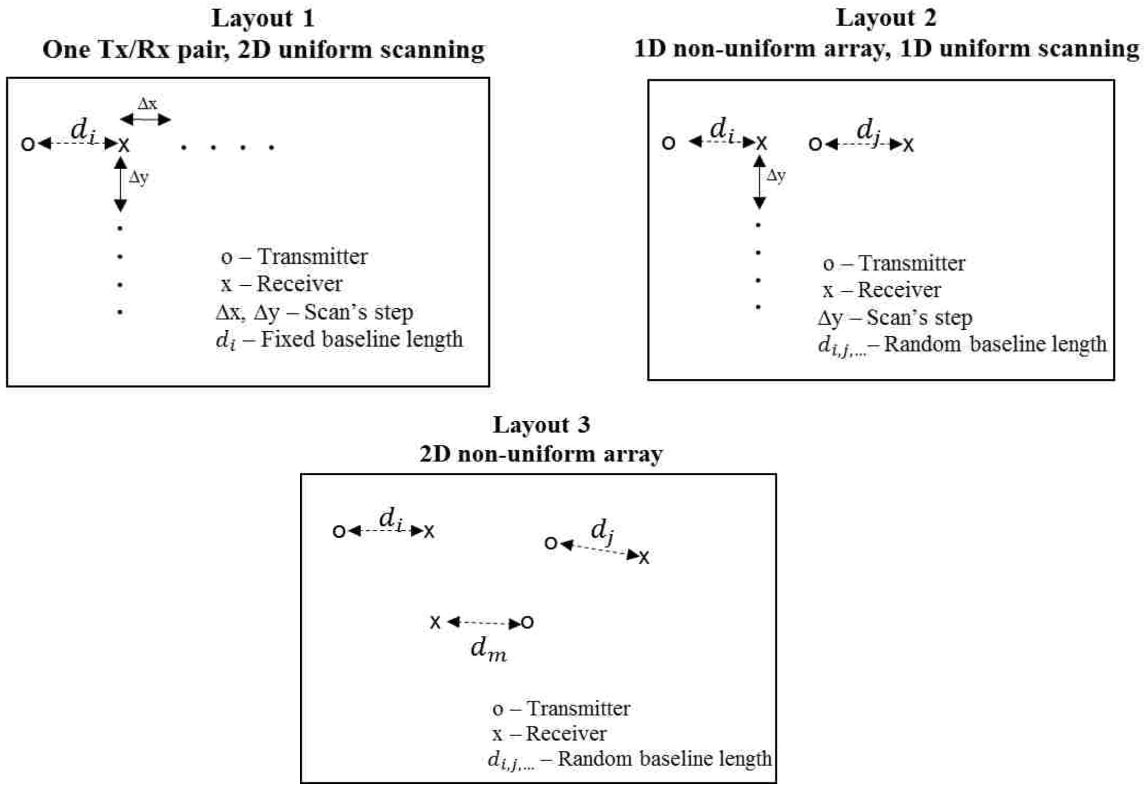

Figure 9. Three imaging system Layouts with different sampling steps and Tx/Rx pair distributions.

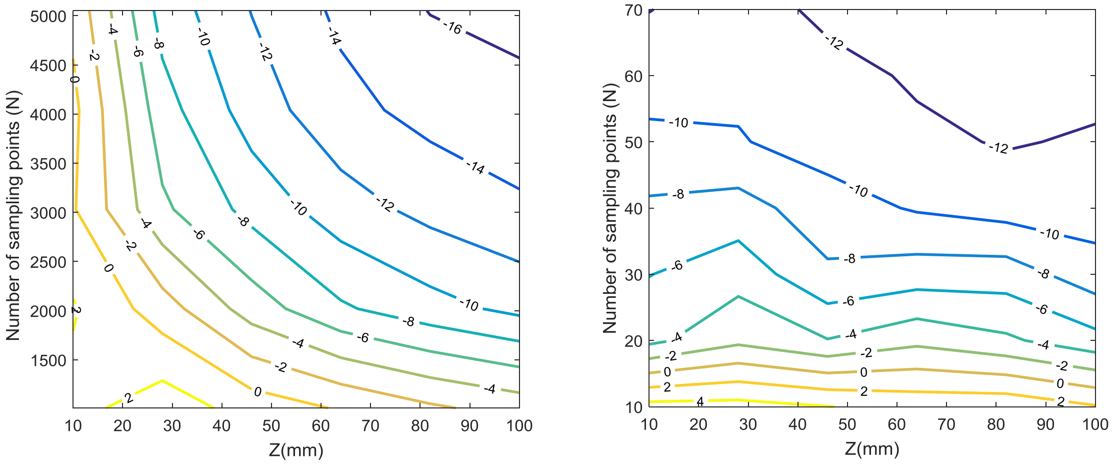

a b

Figure 10. *E* contours in terms of Z and number of sampling points for (a) Layout 2 and (b) Layout 3.

Next, E in terms of d for different Layouts is calculated for the far field (Z = 100 mm) and near field (Z = 40 mm) for an additive noise power of -150 dB to study E as a function of d for a case where the noise power does not affect the error (as mentioned above). The results of the far field imaging are shown in Figure 11. Here, for Layouts with a random baseline length of Tx/Rx pairs (Layouts 2 and 3), the average baseline length is considered as d where baseline length changes randomly (uniform distribution between 7 mm to 20 mm). In Layout 1, 10^4 sampling points are used due to the small spatial sampling step sizes ($\Delta x = \Delta y = 2$ mm) and in Layout 2, with 40 Tx/Rx pairs and $\Delta y = 2$ mm, there are 4×10^3 sampling points. For Layout 3 with the sparse random array, there are 55 sampling points. As shown in Figure 11, for image error $E < -10$ dB, d must be less than ~16 mm for Layouts 1 and 2 and less than ~13 mm for Layout 3. Hence, regardless of each pair's baseline length (even when $2\beta > 10°$ or $Z/d < 6$, as mentioned above), the image quality of Layout 2 is similar to the image quality of Layout 1. This is important when designing imaging arrays since Layout 2 (a 1D imaging array) provides image quality as high a raster scanned system (Layout 1) but with a much shorter imaging time [19]. As such, Layout 2 is considered a compromise between a capability of image quality provided by Layout 1, and image acquisition speed provided by Layout 3. For Layout 3, when the average baseline length is lower than 11 mm (1.1 λ), image quality is similar to that provided by Layout 1.

When considering the near field region as defined by the bistatic baseline length, the error of images reconstructed using the equivalent monostatic model increases drastically. To illustrate this, simulations were conducted for the near field (Z = 40 mm) case with -150 dB additive noise. Here, E in terms of d for different Layouts for near field imaging is shown in Figure 12. The results show that the error increases drastically for near field imaging (*Z/d* < 4) as compared to far field imaging and the effect of the bistatic error for this shorter range on image distortion is more significant; in particular for Layouts 1 and 2. For instance, for far field imaging (*Z* = 100 mm in Figure 12), *E* is less than -10 dB for Layouts 1 and 2 when *d* < 17 mm, while for near field imaging (*Z* = 40 mm in Figure 12) the maximum *d* for negligible image distortion is ~13 mm. For Layout 3 with sparse 2D sampling, image distortion was larger than Layouts 1 and 2 in both cases (far and near fields) for baseline lengths greater than ~1 wavelength. This is as expected due to the importance of the relationship between *d* and λ in near field imaging (as discussed in Section II) and become critical factor in sparse sampling.

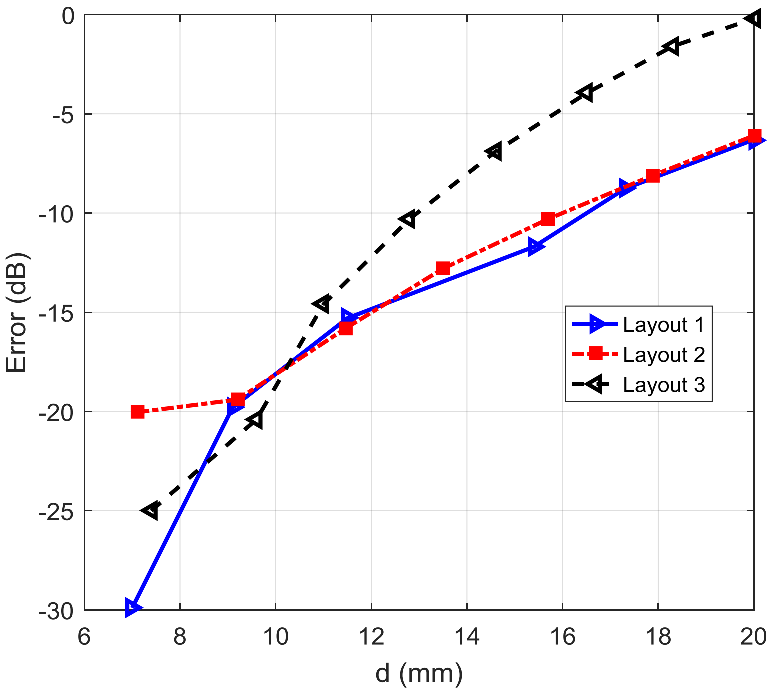

Figure 11. Simulated *E* in terms of baseline length for *Z* = 100 mm for different Layouts.

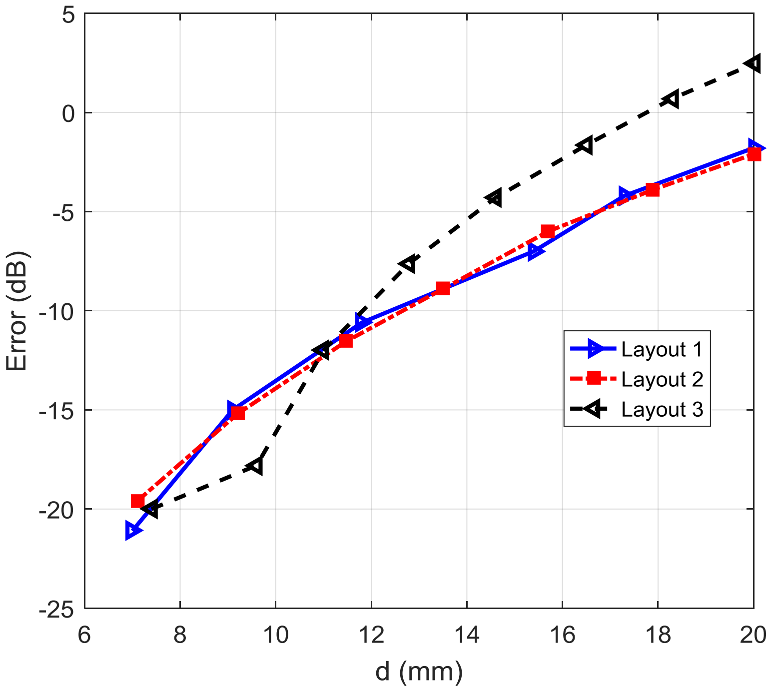

Figure 12. Simulated *E* in terms of baseline length for *Z* = 40 mm for layouts 1, 2 and 3.

5. PHASE COMPENSATION FOR ERROR REDUCTION

Since the image distortion is caused by the phase error due to the approximation of a bistatic scenario with a monostatic model, a phase compensation method is proposed and applied to received backscattered signal (similar to [20]). Since this phase error changes as a function of the relative location of the Tx/Rx pairs and the number of sampling points, the average phase error as defined by the bistatic baseline length and the target range is used. To define the average phase compensation value ($\Delta\varphi_c$), the phase difference defined as $R_T + R_R - 2R$ is approximated by $2R_c$ - $2Z$ as shown in (2), where in (3), R_c is calculated in terms of known parameters of the bistatic configuration (range and baseline length).

Then, calculated is $\Delta\varphi_c$ subtracted from received backscattered signal's phase to compensate phase difference between monostatic model and bistatic configuration.

$$\Delta\varphi_c = 2k(R_c - Z) \tag{2}$$

$$R_c = \sqrt{Z^2 + (d/2)^2} \tag{3}$$

To demonstrate the applicability of this correction method, simulation results for the same scenario discussed in Section IV (scanning over 200 mm × 200 mm aperture plane) are depicted for cases with and without phase compensation for Layouts 1, 2 and 3. In these simulations, additive noise power is assumed to be -75 dB (a realistic additive noise power). In Figure 13(a) and (b), the simulated E contours in terms of Z and d are depicted without and with the phase compensation to the received backscattered signal, using the scenario of Layout 1, where the bistatic baseline length is constant across the imaging aperture. As seen, applying the phase compensation generally improves the image error (contours shifting to the right) except for very large Z, where noise effects become dominant. For example, given a fixed range of Z = 60 mm, the maximum baseline length for negligible image distortion (E < -10 dB) is 13 mm without phase compensation, but with phase compensation, a similar image error can be obtained for baseline lengths up to 18 mm. Similarly, for Layout 2, the phase compensation is applied to improve the image error, as shown in Figure 14. Since in Layout 2, the baseline length across the x-dimension is random, the phase compensation is calculated for each Tx/Rx pair independently. The result is a shift in the contours to the right (similar to Figure 13). For example, at Z = 100 mm and to obtain E < -10 dB, the maximum d (average baseline length in Layout 2) is approximately 11 mm without phase compensation, but with phase compensation, the maximum d becomes ~13.5 mm (see Figure 14(b)). Similar trends can be seen for the simulation of Layout 3, with the E contours for this case shown in Figure 15. However, unlike Layouts 1 and 2, applying phase compensation only improves the image error slightly due to the extreme sparsity of Layout 3.

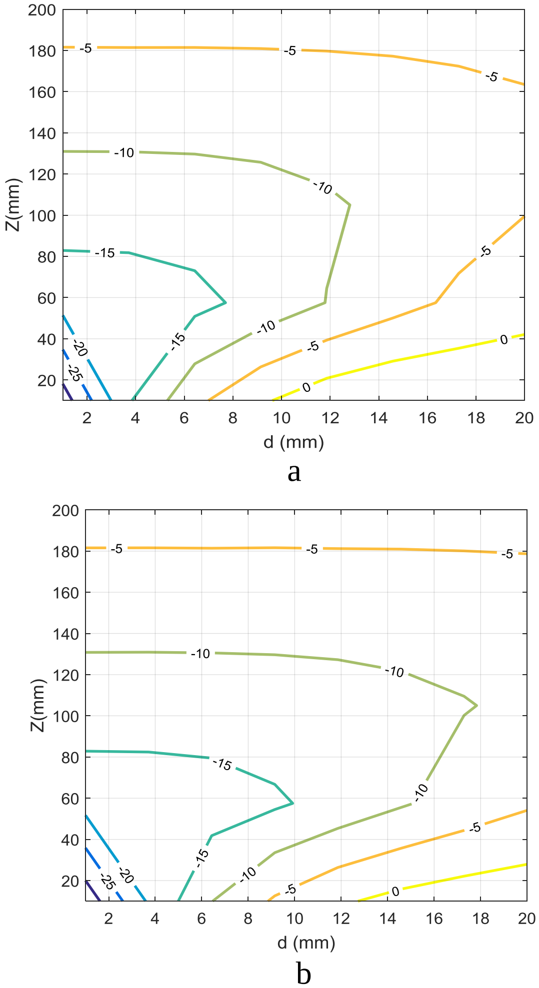

a

b

Figure 13. E contours (dB scale) as a function of Z and d for Layout 1 (a) without phase compensation and (b) with phase compensation.

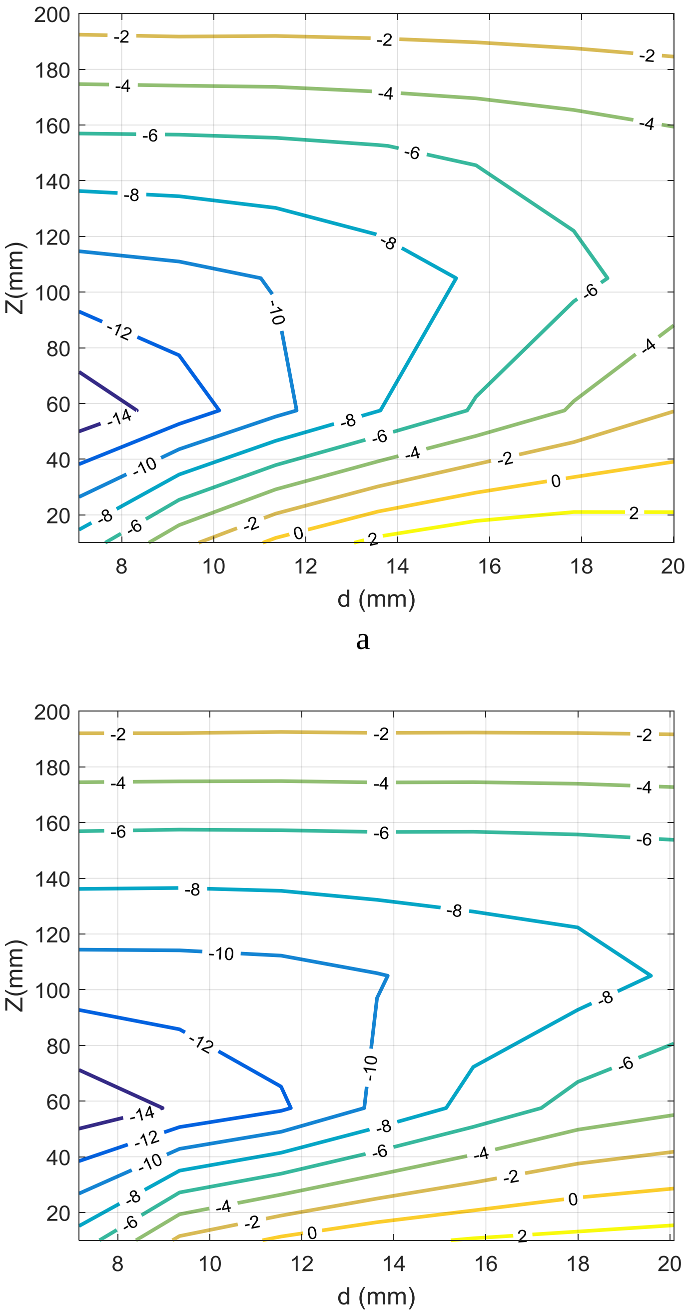

a

b

Figure 14. *E* contours (dB scale) as a function of *Z* and average *d* for Layout 2 (a) without phase compensation and (b) with phase compensation.

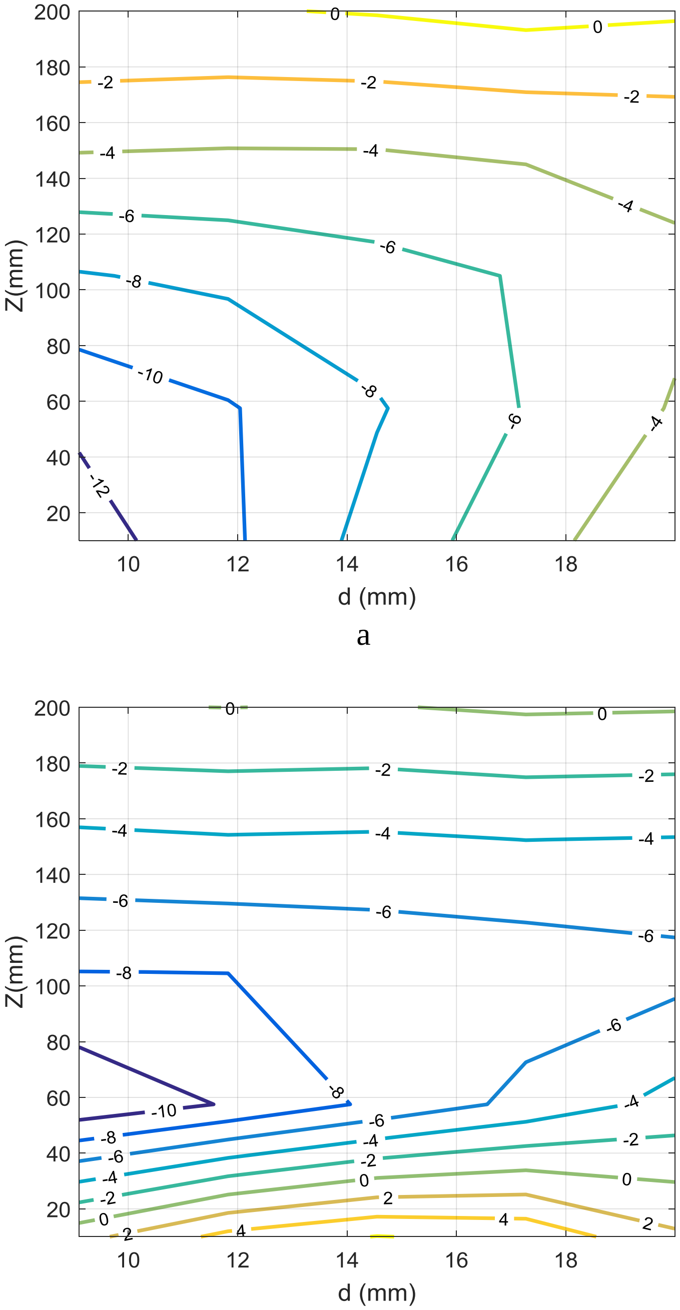

a

b

Figure 15. *E* contours (dB scale) as a function of Z and average d for Layout 3 (a) without phase compensation and (b) with phase compensation.

6. MEASUREMENT RESULTS

To support the simulation results shown above, experiments were conducted using imaging systems represented by Layout 1 and Layout 2, with the error determined and discussed for two scenarios (with and without phase compensation). Here, as was the case for the same measurement setup of Section 3, bistatic measurement results are processed and *E* in terms of *d* is depicted with and without applying phase compensation.

6.1. LAYOUT 1

By 2D raster scanning with different baseline lengths (as shown in Figure 8), measured backscattered signals are collected and processed for both monostatic and bistatic measurements. For both measurements, monostatic SAR is utilized for reconstructing the image of the target (metallic ball). Simulated (for comparison) and measured results of Layout 1 without and with phase compensation are shown in Figure 16. As shown, there is good agreement between the simulated and measurement results. Furthermore, the phase compensation improves the image error by approximately 2 to 3 dB for all baseline lengths.

6.2. LAYOUT 2

Using the setup shown in Figure 7, six scans were performed with different baseline length in the range of 9 to 22 mm. These scans were combined to synthesize a 1D imaging array with non-uniform baseline length. In Figure 17, measurement results before and after applying phase compensation are depicted. As shown, the image error generally improves with phase compensation. For example, the maximum average baseline length for negligible image distortion (E < -10 dB) increases from 10 mm to 12 mm by applying phase compensation.

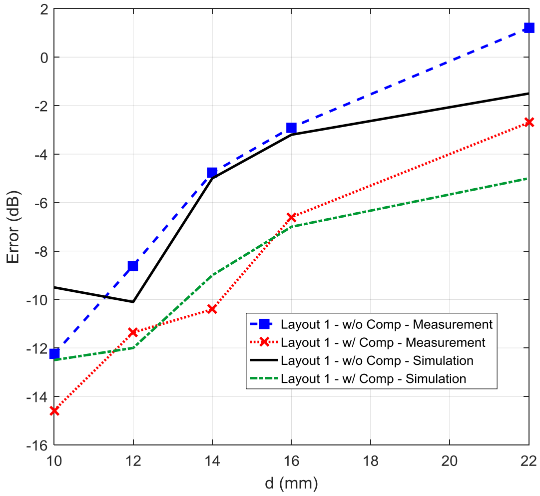

Figure 16. *E* in terms of *d* in Layout 1 for simulated and measured data with and without phase compensation.

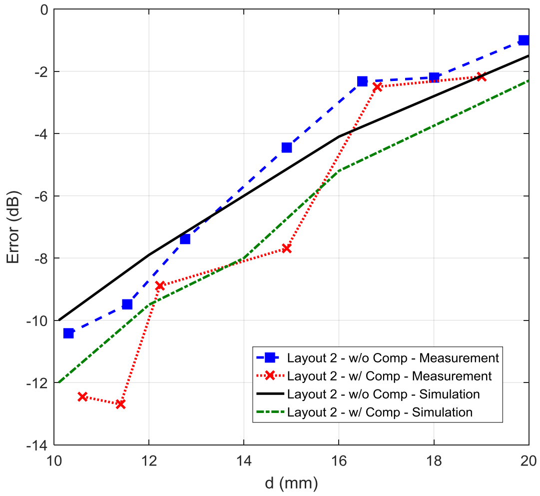

Figure 17. *E* in terms of *d* in Layout 2 for simulated and measured data with and without phase compensation.

7. CONCLUSION

In this work, the image distortion that results from using an equivalent monostatic model for bistatic measurements in SAR imaging was investigated. The monostatic model is preferred for its computational efficiency, yet bistatic measurements are preferred for their sensitivity. The results indicated that low image distortion (quantified through RMS error) can be obtained when the bistatic baseline length is small (approximately one wavelength or smaller), or when the range is much larger than the baseline length. The results also showed that additive noise power becomes the main contributor to the image error when the range is large. The simulated and measured results showed good agreement with slight discrepancies. In order to fully investigate the image distortion that results from the application of a monostatic model to bistatic SAR measurements, additional simulations and measurements were conducted for different layouts of Tx/Rx pairs, therein simulating raster scanning and non-uniform imaging arrays. The results show that for imaging systems with random baseline lengths (on the order of 10 mm (λ) to 20 mm (2λ)), the image distortion due to the equivalent monostatic model can meet the criteria of $E < -10$ dB and is negligible for an optimized number of sampling points and average baseline length. Also, the results show that the effect of the number of sampling points on image quality is more significant in near field imaging as compared to far field imaging. Moreover, by applying phase compensation to minimize phase differences between bistatic measurement and monostatic model, the image error is improved.

REFERENCES

J. T. Case, F. L. Hepburn, R. Zoughi, "Inspection of Spray on Foam Insulation (SOFI) Using Microwave and Millimeter Wave Synthetic Aperture Focusing and Holography," in Instrumentation and Measurement Technology Conference, 2006. IMTC 2006. Proceedings of the IEEE, 2006, pp. 2148-2153.

J. T. Case, M. T. Ghasr, R. Zoughi, "Optimum Two-Dimensional Uniform Spatial Sampling for Microwave SAR-Based NDE Imaging Systems," IEEE Trans. Instrum. Meas., vol. 60, pp. 3806-3815, 2011.

J. T. Case, S. Kharkovsky, R. Zoughi, and F. Hepburn, "High Resolution Millimeter Wave Inspecting of the Orbiter Acreage Heat Tiles of the Space Shuttle," in Instrumentation and Measurement Technology Conference Proceedings, 2007. IMTC 2007. IEEE, 2007, pp. 1-4.

M. T. Ghasr, Kuang P. Ying ,Reza Zoughi," SAR imaging for inspection of metallic surfaces at millimeter wave frequencies", Instrumentation and Measurement Technology Conference (I2MTC) Proceedings, 2014 IEEE International,july 2014.

M. Pastorino, Microwave imaging vol. 208: John Wiley & Sons, 2010.

D. M. Sheen, D. L. McMakin, and T. E. Hall, "Three-dimensional millimeter-wave imaging for concealed weapon detection," IEEE Trans. Microw. Theory Tech., vol. 49, pp. 1581-1592, 2001.

Joseph T. Case, Mohammad Tayeb Ghasr, and Reza Zoughi, "Optimum Two-Dimensional Uniform Spatial Sampling for Microwave SAR-Based NDE Imaging Systems", IEEE TRANSACTIONS ON Instrumentation and Measurement, VOL. 60, NO. 12, December2011.

M. Soumekh, "Bistatic Synthetic Aperture Radar Inversion with Application in Dynamic Object Imaging," IEEE Transactions on Signal Processing Vol.39, pp.2044 - 2055, Sep 1991.

Y. Wu, Y.Huang, X.Wu, "A equivalent monostatic imaging algorithm for bistatic synthetic aperture radar," Synthetic Aperture Radar, 2007. APSAR 2007. 1st Asian and Pacific Conference on, January 2008.

Ender, J., I. Walterscheid, A. Brenner, "New aspects of bistatic SAR: Processing and experiments," Proc. of IGARSS, 1758-1762, 2004.

Wong, F. H. and T. S. Yeo, “New applications of nonlinear chirp scaling in SAR data processing," IEEE Trans. Geosci. Remote Sens, Vol. 39, No. 5, 946-953, 2001.

Z.Wu, X. Zhang, X.Wu,” A Novel Wavenumber Domain Algorithm for Bistatic SAR Imaging Based on Equivalent Monostatic Model”, Progress In Electromagnetics Research M, Vol. 45, 113–121, 2016.

Z. Manzoor, M. T. Ghasr, K. M. Donnell. "Image distortion characterization due to equivalent monostatic approximation in near field bistatic SAR imaging.", *Instrumentation and Measurement Technology Conference (I2MTC), 2017 IEEE International*, pp. 1-5, 2017.

Z. Manzoor, M. T. Ghasr, K. M. Donnell. "Image distortion characterization due to equivalent monostatic approximation in near field bistatic SAR imaging.", *Instrumentation and Measurement Technology Conference (I2MTC), 2017 IEEE International*, pp. 1-5, 2017.

M. T. Ghasr, M. J. Horst, M. R. Dvorsky and R. Zoughi, "Wideband Microwave Camera for Real-Time 3-D Imaging," *IEEE Transactions on Antennas and Propagation*, vol. 65, no. 1, pp. 258-268, Jan. 2017.

M. T. Ghasr, S. Kharkovsky, R. Bohnert, B. Hirst and R. Zoughi, "30 GHz Linear High-Resolution and Rapid Millimeter Wave Imaging System for NDE," *EEE Transactions on Antennas and Propagation*, vol. 61, no. 9, pp. 4733-4740, Sept. 2013.

X. M. Peng, Y.P. Wang, H. Wen, W.X. Tan, Y.R. Wu, "Airborne Downward Looking Sparse Linear Array 3-D SAR Heterogeneous Parallel Simulation", *Remote Sens.*, vol. 5, pp. 5304-5329, 2013.

III. A COMPREHENSIVE BI-STATIC AMPLITUDE COMPENSATED RANGE MIGRATION ALGORITHM (AC-RMA)

ABSTRACT

In this paper, a comprehensive form of the range migration algorithm (RMA) is analytically derived for reconstructing the reflectivity function in imaging systems. More specifically, amplitude compensation, in addition to the typical phase compensation, is included in the development of the matched filter of the RMA, and is herein referred to as the amplitude compensated RMA (AC-RMA). To illustrate the improvements offered by the AC-RMA, simulations and measurement (at Ka-band, 26.5 – 40 GHz) are performed to reconstruct the reflectivity function of a target using both RMA and AC-RMA algorithms. The results prove that the AC-RMA is a robust algorithm that can successfully reconstruct the reflectivity function of a target with higher accuracy, regardless of its dielectric properties, including scenarios with low contrast between the dielectric properties of the background and target in the presence of noise. This approach is also independent of the bandwidth of the imaging system and is applicable to multilayer media as well. In addition, while the formulation of the AC-RMA is more complicated than the traditional (phase compensation only) RMA, the processing time necessary for images created with the AC-RMA is just 1.2 times greater than that of the traditional RMA processing time.

1. INTRODUCTION

In order to achieve high resolution images for nondestructive evaluation (NDE), synthetic aperture radar (SAR) is known as a well-developed technique. Within this technique, many algorithms are used that incorporate different approximations to reconstruct reflectivity functions, or images, of objects from measured backscattered signals [1]-[6]. For instance, in strip map-mode SAR, the Fresnel approximation is used to reconstruct the reflectivity function from the received signal that is assumed to resemble a spherical wave and is applicable to far-field imaging distances [3]. However, for applications where the target is in the near field of the synthetic aperture of the imaging system, this approximation is not valid. Unlike strip map-mode SAR, in spotlight-mode SAR, a plane wave assumption is used in order to decompose the spherical waves radiated by the transmitting antenna and received by the receiving antenna into a superposition of plane wave components [4]-[6]. Spotlight-mode SAR can be used in the near and far fields of the synthetic aperture, but high image quality is obtained only for large targets in the far field region. In the range migration algorithm (RMA) or ω-k algorithm, since actual spherical waves are considered, image quality increases, regardless of target size and location [5], [7]. In this algorithm, the received signal is described by the convolution of the reflectivity function and point spread function, or PSF, which describes the response of the imaging system to a point source [8]. This convolution can be implemented in the Fourier (spectral) domain as a complex product to reduce computational complexity. Hence, as explained in [8], the spectral reflectivity function of the target is defined as multiplication of the spectral received signal and a matched filter, which is derived in terms of the PSF in the spectral domain (defined as the inverse PSF). In [8], the PSF is defined based on the free space Green’s function, and Weyl’s definition [9], which includes phase change and amplitude decay as a function of target range. Hence, in the defined matched filter, phase and amplitude correction should be applied to compensate for the PSF effect (i.e. amplitude decay and phase change). In previous works such as [7], [8] and [10], the amplitude decay is ignored in the matched filter based on the assumption that it has a negligible effect on the image quality (as compared to the phase effect). However, this assumption does not hold for all cases, including those where the dielectric properties of the target and background are similar (i.e. low contrast), in particular when the signal-to-noise ratio (SNR) is low. This means that disregarding the amplitude decay of the matched filter causes the image quality to degrade drastically, and in low SNR scenarios, the target cannot be distinguished from the background. Therefore, in this work, the complete form of the matched filter is derived for the RMA algorithm, in which both phase and amplitude compensations are defined precisely. The RMA algorithm with this complete form of the matched filter is herein referred to as the amplitude compensated-RMA (AC-RMA). To this end, this work provides the formulation of the AC-RMA, along with simulations and measurements to illustrate the improvement offered by this updated algorithm. In addition, the reflectivity function of a target obtained by the RMA and AC-RMA algorithms is compared for narrow- and wideband operation. Such a comparison is useful since the SAR algorithm is commonly used for narrowband operation. However, wideband operation facilitates a significant improvement in the range resolution of the image [11]. In addition, the efficacy of RMA and AC-RMA is studied with respect to the reconstruction of reflectivity functions of targets located in layered media. Lastly, measurements were performed for a worst case scenario (bistatic imaging system with around two wavelengthlarge baseline length (distances between the transmitting and receiving antennas) [12] - [13]) to examine the efficacy of the AC-RMA when a bistatic setup cannot be approximated by an equivalent monostatic model [14]. To this end, Ka-band waveguide antennas, as the transmitter/receiver (Tx/Rx) pair, were used to scan a dielectric target. Measurement results illustrate that the AC-RMA can reconstruct the image more accurately than the RMA.

2. FORMULATION

To derive the general formulation of the AC-RMA for SAR imaging systems, a bistatic is considered (such as that of [13]) and illustrated in Figure 1. More specifically, the aperture of the imaging system is located at $z = 0$, with the transmitter located at (x_t, y_t, 0), and the receiver located at (x_r, y_r, 0). Also, a general point on the target is assumed at position $O(x, y, z)$, and reflectivity function, $f(x, y, z)$, is used to characterize the target.

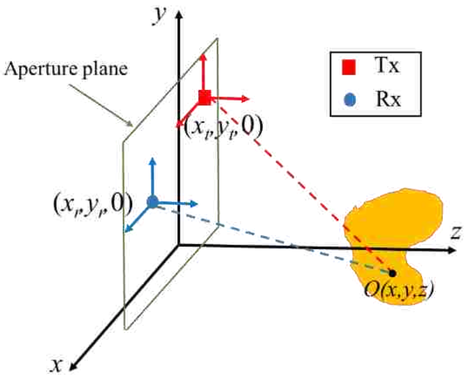

Figure 1. Illustration of a general bistatic imaging configuration.

The received signal is denoted as $s(x_t, y_t, x_r, y_r, k)$ and is measured at the aperture plane. Here, $k = \omega\sqrt{\mu\varepsilon}$ is the wavenumber and is a function of angular frequency (ω), permittivity (ε), and permeability (μ) of the media. Generally speaking, $s(x_t, y_t, x_r, y_r, k)$ is the response of the superposition of each point on the target multiplied by the two-way (roundtrip) three dimensional (3D) free space Green's function (as discussed in [7] and [13]) and is given as:

$$s(x_t, y_t, x_r, y_r, k) = \iint f(x, y) g(R_t, k) g(R_r, k) dxdy \tag{1}$$

Where the free space transmits and receive Green's functions are defined as:

$$g(R_t, k) = \frac{-1}{8\pi k R_t} \mathrm{e}^{(-jkR_t)} \tag{2}$$

$$g(R_r, k) = \frac{-1}{8\pi k R_r} \mathrm{e}^{(-jkR_r)} \tag{3}$$

In Equation (1), (2) and (3), R_t and R_r are the distances between any point on the target and the transmitter and receiver antennas, respectively, and are defined as $R_t = \sqrt{(x - x_t)^2 + (y - y_t)^2 + z^2}$ and $R_r = \sqrt{(x - x_r)^2 + (y - y_r)^2 + z^2}$. By defining R_0 as the midpoint of the bistatic baseline length (the distance between the transmitter (Tx) and receiver (Rx)), Equation (1) can be reformulated to Equation (4) as a two dimensional (2D) convolution and frequency integration.

$$s(x_t, y_t, x_r, y_r, k) = \\ f(x, y) * g(R_t, k) * g(R_r, k) \tag{4}$$

The 2D convolution can be computed per frequency in the Fourier (spectral) domain as a complex product, as shown in Equation (5).

$$S(k_{xt}, k_{xr}, k_{yt}, k_{yr}, k) = \\ F(k_{xt}, k_{xr}, k_{yt}, k_{yr}, k) G(k_{xt}, k_{yt}, k) G(k_{xr}, k_{yr}, k) \tag{5}$$

Here, the spectral received signal and reflectivity functions are referred to as $S(k_{xt}, k_{xr}, k_{yt}, k_{yr}, k)$ and $F(k_{xt}, k_{xr}, k_{yt}, k_{yr}, k_0)$, respectively. In addition, $k_{xt/r}$ and $k_{yt/r}$ are the spectral wavenumbers corresponding to $x_{t/r}$ and $y_{t/r}$, and they are linked together by equations expressed in [13]. Additionally, the spectral round-trip Green's function is denoted as $G(k_{xt}, k_{yt}, k)G(k_{xt}, k_{yt}, k)$ and can be analytically expressed under certain conditions for which integrals with rapidly varying phase terms can be evaluated using the method of stationary phase (MSP), as discussed in [7]. As mentioned in [7], based on the MSP, stationary points (nulls of the phase derivative) of the integral are the main contribution of the outcome of the integral. Hence, by applying the MSP, $G(k_{xt}, k_{yt}, k)G(k_{xt}, k_{yt}, k)$ can be completely (without approximations) defined as Equation (6), in which both amplitude and phase of PSF (i.e., the round-trip spectral Green's function) is considered (see the Appendix for the full derivation). A last point to be noted is that while the more general bistatic formulation is considered here, the final AC-RMA formulation can be modified for a monostatic configuration by considering the transmitter and receiver to be collocated.

$$S(k_{xt},k_{xr},k_{yt},k_{yr},k)/F(k_{xt},k_{xr},k_{yt},k_{yr},k)= \tag{6}$$

$$\left(\frac{e^{j\Phi(x_t^0,x_r^0,y_t^0,y_r^0)}}{(4\pi)^2R_t(x_t^0,y_t^0)R_r(x_r^0,y_r^0)}.e^{j\pi/4}\right).$$

$$\left(\begin{array}{l}
8a^2b\sqrt{\dfrac{2\pi}{\left|\Phi_{y_ry_r}(x_r^0,y_r^0)\right|}}+8b^2a\sqrt{\dfrac{2\pi}{\left|\Phi_{x_rx_r}(x_r^0,y_r^0)\right|}}+\\
8a^2b\sqrt{\dfrac{2\pi}{\left|\Phi_{y_ty_t}(x_t^0,y_t^0)\right|}}+8b^2a\sqrt{\dfrac{2\pi}{\left|\Phi_{x_tx_t}(x_t^0,y_t^0)\right|}}+\\
4(a-x_t^0)Si\left[(a-x_t^0)(b-y_t^0)\Phi_{y_tx_t}(x_t^0,y_t^0)\right]+\\
4(a-x_r^0)Si\left[(a-x_r^0)(b-y_r^0)\Phi_{y_rx_r}(x_r^0,y_r^0)\right]
\end{array}\right)$$

Where:

$$\Phi(x_t,x_r,y_t,y_r)=-kR_t-kR_r-k_{xr}x_r-k_{xt}x_t-k_{yt}y_t-k_{yr}y_r \tag{7}$$

$$x_{t/r}^0=\frac{k_{zt/r}.x-k_{xt/r}.z}{k_{zt}} \tag{8}$$

$$y_{t/r}^0=\frac{k_{zt/r}.y-k_{yt/r}.z}{k_{zt/r}} \tag{9}$$

$$R_{t/r}{}^0=\frac{-k.z}{k_{zt/r}} \tag{10}$$

$$\Phi_{y_{t/r}y_{t/r}}=\frac{-k_{zt/r}}{z}-\frac{k_{yt/r}.k_{zt/r}{}^2}{k^2.z^2} \tag{11}$$

$$\Phi_{x_{t/r}x_{t/r}}=\frac{-k_{zt/r}}{z}-\frac{k_{xt/r}.k_{zt/r}{}^2}{k^2.z^2} \tag{12}$$

$$\Phi_{y_{t/r}x_{t/r}}=\frac{k_{xt/r}.k_{zt/r}.k_{yt/r}}{k^2.z}. \tag{13}$$

Here, to derive the PSF (as defined in the Appendix) (x_t^0, y_t^0) and (x_r^0, y_r^0) are described as stationary points where $\Phi(x_t, y_t, x_r, y_r)$ has an extreme value. These stationary points are expressed based on k_{zt} and k_{zr}, which are defined from the dispersion relation as described in [13]. Lastly, the matched filter $1/[G(k_{xt}, k_{yt}, k)G(k_{xt}, k_{yt}, k)]$ can be derived to obtain the spectral reflectivity function and then the 3D reconstructed image can be found by applying an inverse Fourier transform to the spectral reflectivity function. This process is illustrated in the block diagram of Figure 2.

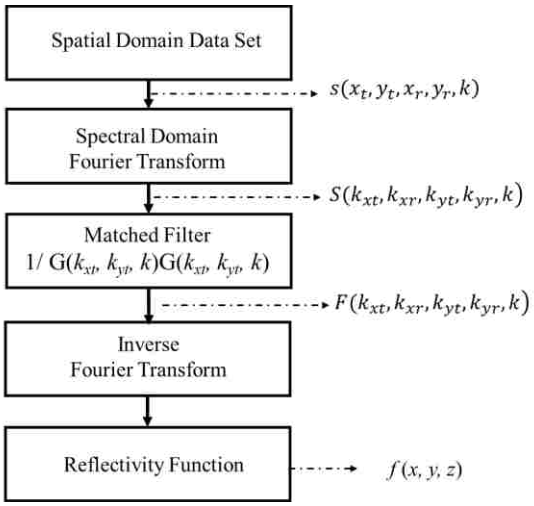

Figure 2. Block diagram of the AC-RMA.

3. SIMULATION RESULTS

Here, the efficacy of the proposed AC-RMA to reconstruct the reflectivity function of dielectric targets with a background of low dielectric (specifically permittivity) contrast at Ka-band (26.5 - 40 GHz) frequencies is studied through simulation. Since such reconstructions are even more challenging when the received signal is low (or on the order of the noise power, rendering a low SNR), white Gaussian noise was added to the simulations. To this end, the reconstructed reflectivity function of a rectangular dielectric target embedded in a dielectric background is calculated for different target and background permittivities and additive noise powers using the AC-RMA and RMA algorithms. The target has dimensions of 4 × 4 mm2 (less than λ/2 × λ/2 at the mid-band frequency of Ka-band, where λ is the wavelength of the operating frequency in free space). For this reconstruction, bistatic pairs of transmitters and receivers are located arbitrarily in a 50 × 50 mm2 (~5λ × 5λ) aperture plane with random baseline length (i.e., non-uniform sampling of the backscattered signal as described in [2]). Here, non-uniform sampling is chosen to reduce the number of required spatial samples, resulting in minimal image processing time without disturbing image quality [2]. Hence, in such an imaging system, to minimize the number of sampling points, the Tx/Rx pair baseline length and consequently the number of pairs must be optimized in order to reconstruct the reflectivity function (i.e., images) with high image quality (as is discussed later). To this end, similar to [14], the root-mean-square (RMS) error (E) of the reconstructed reflectivity function by RMA and AC-RMA for different Tx/Rx pairs numbers is calculated when the actual reflectivity function of a known target is used as the reference reflectivity function. As justified in [14], an E less than -10 dB is acceptable for negligible image distortion. Hence, for different Tx/Rx pairs, E is calculated for both RMA and AC-RMA algorithms and is shown in Figure 3 for different target ranges (Z) with -75 dB additive white Gaussian noise power added to the received signal as described in [14]. An average baseline length of 10 mm is used for this simulation. As seen in Figure 3(a), for this single point target, the RMA algorithm can reconstruct the target's reflectivity function with acceptable error (meaning E < -10 dB) when Z is larger than 80 mms, independent of the number of Tx/Rx pairs. However, for the AC-RMA (Figure 3(b)), there is an average of 6 dB improvement in E which becomes less than -10 dB for Z < 20 mm and indepdent of number of Tx/Rx pairs. Therefore, for all other following simulated reflectivity functions in this paper, Z = 100 mm for both RMA and AC-RMA algorythms is considred to achieve $E < -10$ dB for 10 Tx/Rx pairs and an average sampling step size in both x and y directions of ~15 mm. For reconstructing the reflectivity function for this number of Tx/Rx pairs, a computer with an Intel (R) Xeon (R) CPU E5-2630 and 32 GB of RAM is used for processing. With this computer, the AC-RMA and RMA algorithms require 1.423 and 1.255 seconds, respectively, for reconstructing the images from data with 1 GHz bandwidth with a step size of 100 MHz.

For comparison of the ability of the RMA and AC-RMA algorithms to reconstruct the reflectivity function, in Figure 4, simulated reflectivity functions (normalized with respect to maximum amplitude) are shown. Simulations are prepared for targets with a relative permittivity (ε_{r_target}) of 5 in a background permittivity ($\varepsilon_{r\_background}$) of 2.5 to represent a high contrast scene, and ε_{r_target} of 3 in the same background of $\varepsilon_{r\_background} = 2.5$ to represent a low contrast scene (all lossless materials). Simualtions were performed for a center operating frequency of 36.5 GHz with 1 GHz bandwidth and 100 MHz step size. Initially, the scattered wave $s(x_t,y_t,x_r,y_r,k)$ is cacluated using a defined reflectivity function (based on the Born approximation and plane wave reflectivity) and equations (1) - (4). Noise was then added to this scattered wave and then processed using the RMA and AC-RMA to generate images of the reflectivity functions. Comparing the two images obtained using the RMA (Figure 4(a)) and 4(b)), the image quality from the low contrast scene is much lower than the quality of the image for the high contrast scene (Figure 4(b)). On the contrary, for both contrast scenarios, the quality of the images (Figure 4(c) and (d)) obtained using the AC-RMA is comparable and much higher than that of the RMA images.

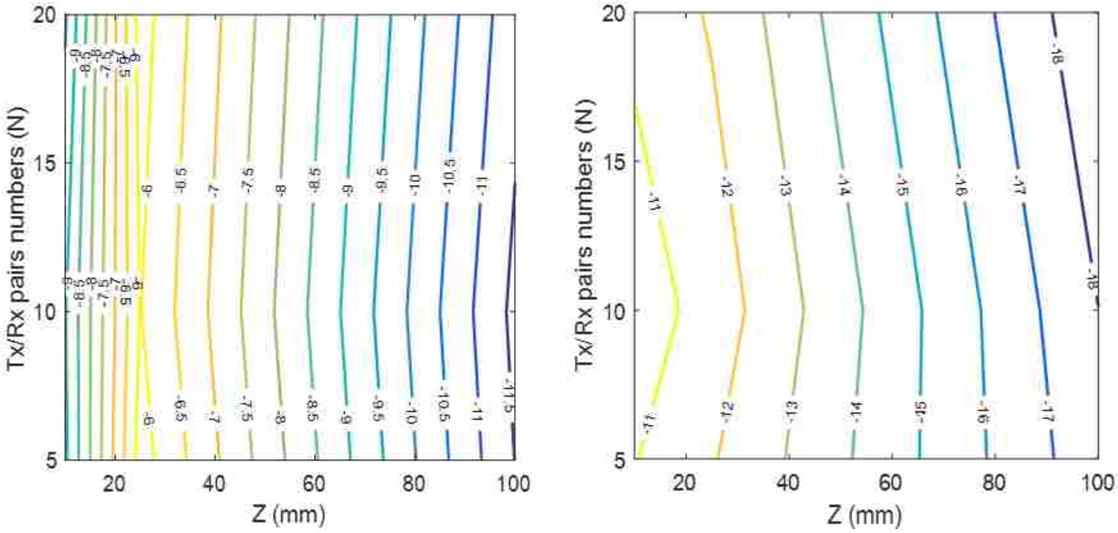

a b

Figure 3. *E* in terms of number of Tx/Rx pairs and target range for (a) RMA and (b) AC-RMA.

Next, to consider the effect of additional noise (i.e., low SNR), the same simulations were conducted but with a noise power of -50 dB. The simulated images obtained using both algorithms are depicted in Figure 5 (for the same target and background permittivity contrasts as those of Figure 4).

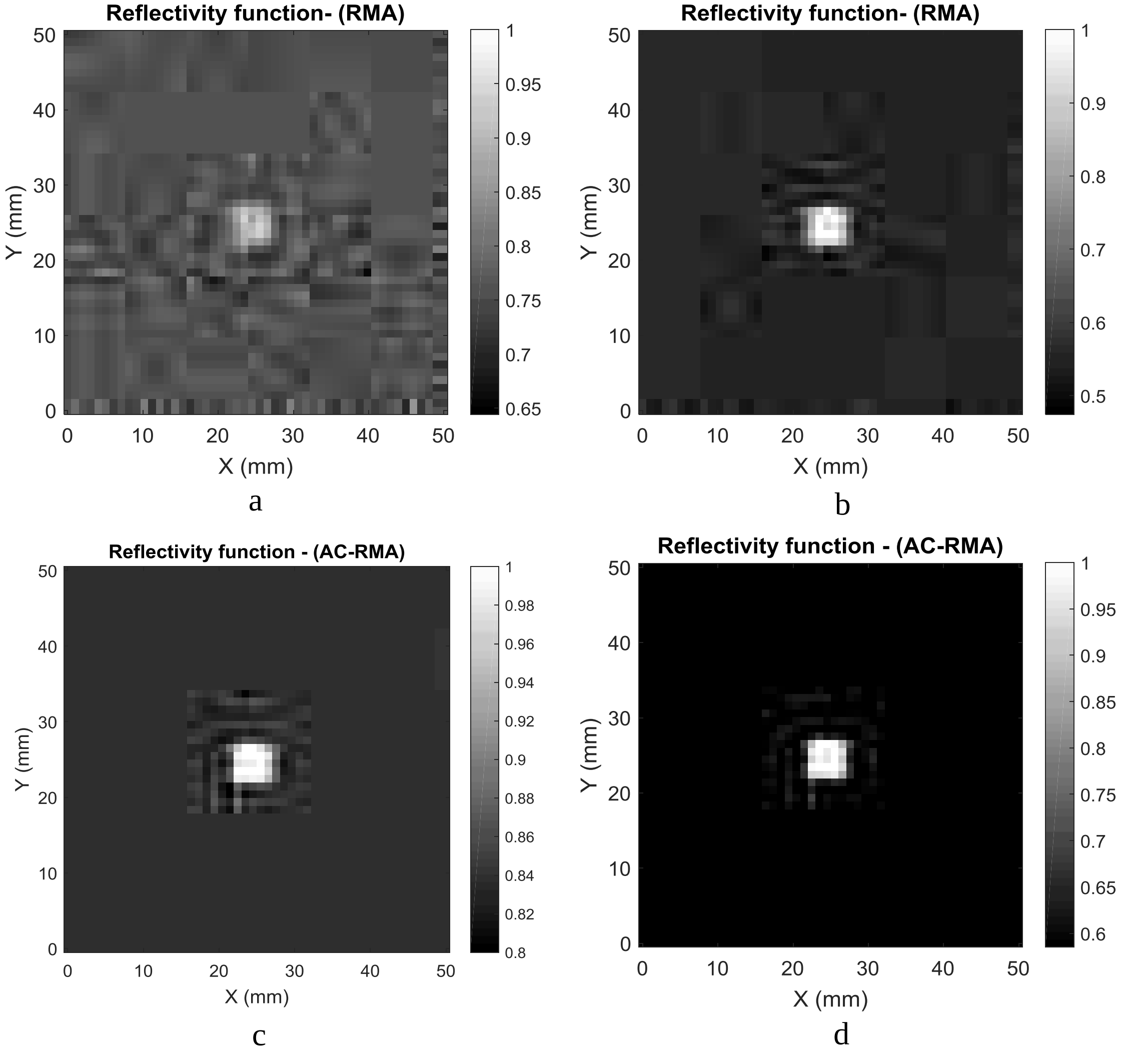

a b

c d

Figure 4. Reconstructed reflectivity function with -75 dB additive noise power when (a) $\varepsilon_{r\_target} = 3$, $\varepsilon_{r\_background} = 2.5$ and (b) $\varepsilon_{r\_target} = 5$, $\varepsilon_{r\_background} = 2.5$ using the RMA, and (c) $\varepsilon_{r\_target} = 3$, $\varepsilon_{r\_background} = 2.5$ and (d) $\varepsilon_{r\_target} = 5$, $\varepsilon_{r\_background} = 2.5$ using the AC-RMA.

As shown in Figure 5, the images obtained using the RMA are much noisier than those in Figure 4, as is expected due to the higher additive nosie power. Specifically, for the low contrast case (Figure 5(a)), the target is not distinguishable and is dominated by noise. In Figure 5(b), the image is noisy but the target remains visible due to its high contrast scene. On the contrary, when using the AC-RMA, regardless of the target and background contrast and signal noise level, the target is clearly visible with a significant reduction in image noise as shown in Figure 5(c) and 5(d).

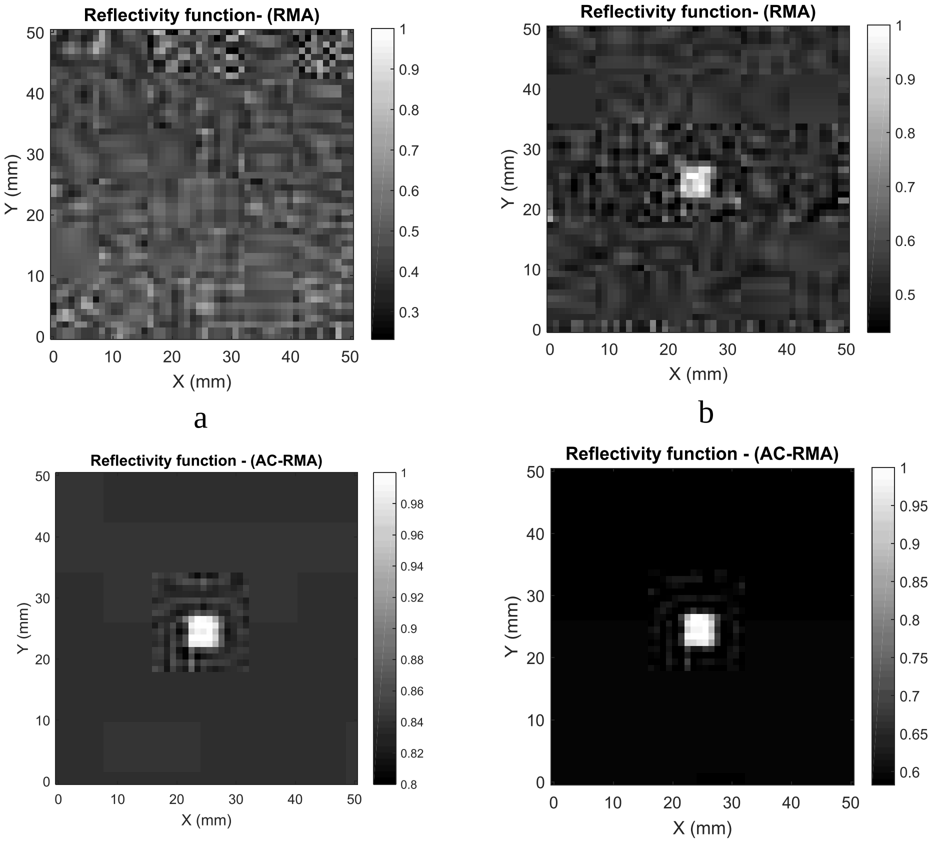

a b

c d

Figure 5. Reconstructed reflectivity function with -50 dB additive noise power when (a) $\varepsilon_{r\_target} = 3$, $\varepsilon_{r\_background} = 2.5$ and (b) $\varepsilon_{r\_target} = 5$, $\varepsilon_{r\_background} = 2.5$ with RMA. (c) $\varepsilon_{r\_target} = 3$, $\varepsilon_{r\_background} = 2.5$ and (d) $\varepsilon_{r\_target} = 5$, $\varepsilon_{r\_background} = 2.5$ with AC-RMA.

Next, to study the effect of bandwidth on the image quality produced by the RMA and AC-RMA algorithms, for a 1 GHz narrow bandwidth (less than 10% of Ka-band), the reflectivity functions reconstructed using both algorithms are simulated, and the results compared with the same reflectivity functions reconstructed using a 13.5 GHz bandwidth (full Ka-band) approach (with a 100 MHz step size). To this end, the target with ε_{r_target} = 5 and background with $\varepsilon_{r\_background}$ = 2.5 located 100 mm away from the imaging aperture is reconstructed when additive Gaussian noise power is -50 dB. In Figure 6(a), the reconstructed reflectivity function of the target by the RMA algorithm with 1 GHz bandwidth (36 – 37 GHz) is shown (same as Figure 5(b)). Figure 6(b) is the reflectivity function reconstructed by the RMA algorithm but with a full Ka-band bandwidth. As shown, for a narrower bandwidth, the RMA algorithm provides better image quality in the reconstructed reflectivity function than for larger bandwidth. However, as depicted in Figure 6(c) and (d), the resolution of the reconstructed reflectivity function by the AC-RMA algorithm (unlike the RMA) is independent of bandwidth. This lack of dependency on bandwidth in the AC-RMA algorithm is related to the AC-RMA matched filter equation. More specifically and as mentioned, in the AC-RMA, the matched filter is derived exactly (without approximation). Hence, as seen in Equation (5), all wavenumbers (k, k_{zt}, k_{zr}, etc.), which are a function of frequency, are considered in the matched filter. In this way, regardless of the bandwidth (number of frequencies that are utilized in the reconstruction), the reflectivity function can be reconstructed with high quality (less image distortion).

In Figure 7, the reflectivity function reconstructed by the RMA and AC-RM are depicted when both target and background permittivity increases dramatically but the ratio of $\varepsilon_{r\_target}/ \varepsilon_{r\_background}$ remains the same as the previous simulations. The target range and additive noise power remain as above (100 mm and -50 dB, respectively). The reflectivity functions are reconstructed by processing the received signal from 36 to 37 GHz.

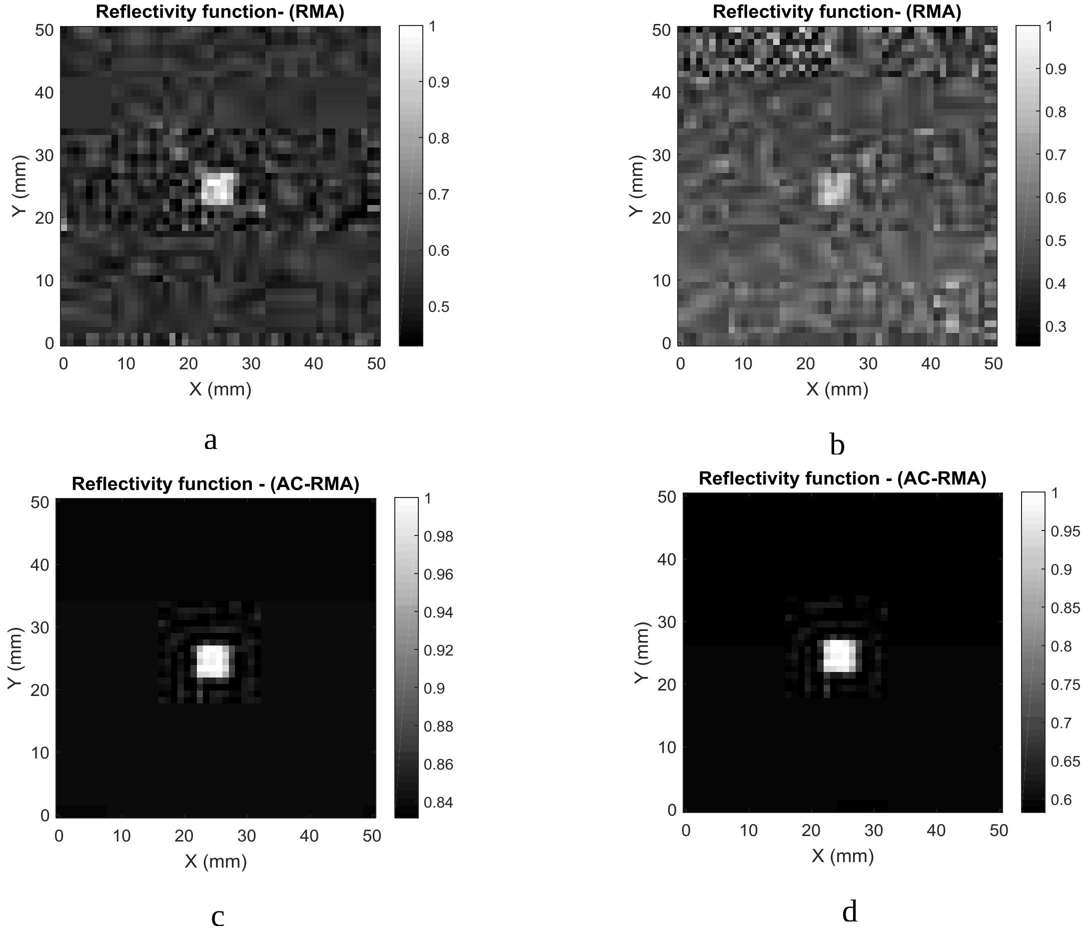

Figure 6. Reconstructed reflectivity function with -50 dB additive noise power for ε_{r_target} = 5, $\varepsilon_{r\_background}$ = 2.5 when bandwidth is (a) 1 GHz (b) 13.5 GHz (Ka-band) with RMA. (c) 1 GHz and (d) 13.5 GHz with AC-RMA.

As seen in Figure 7(a), for the low contrast scenario (ε_{r_target} = 24 and $\varepsilon_{r\_background}$ = 20), the target cannot be distinguished from background noise in the reflectivity function reconstructed using the RMA algorithm. However, for the high contrast scenario (ε_{r_target} = 40 and $\varepsilon_{r\_background}$ = 20), the image quality of the reflectivity function reconstructed by RMA algorithm increases, as shown in Figure 7(b). Further, the image distortion in the reflectivity function reconstructed by the AC-RMA algorithm for both low and high contrast scenarios is negligible, as depicted in Figure 7(c) and (d). Hence, regardless of the permittivityof the target and background, the AC-RMA has the ability to reconstruct the reflectivity function with a low SNR with acceptable image quality.

Next, the efficacy of the RMA and AC-RMA algorithms for reconstructing the reflectivity function of a target in multilayered dielectric media is examined by including the effect of multilayer media on the roundtrip Greens function as discussed in [15]. The importance of reconstructing the reflectivity function of targets within multilayered media becomes clear when applications including detecting defects (targets) such as an air gap between inner layers of a multilayer composite structure are considered [16]. Therefore, in order to examine the efficacy of the RMA and AC-RMA algorithms for detecting targets within multilayered media, the reflectivity function of a square target with a relative permittivity of 2 with an air gap around it at the interface of two different dielectric layers, as shown in Figure 8, is reconstructed.

Multiple simualtions were performed using a cover layer with ε_{r1} = 2.5 and 10 mm thickness (d) which is placed over the background with ε_{r2} which contains a 10 mm × 10 mm square target with ε_{r4} surrounded by 20 mm × 20 mm air gap (ε_{r3} = 1). This structure was located 100 mm away from the aperture plane of the imaging system. In the first simulation, the relative permittivity of the background is chosen larger than the relative permittivity of the square target and the cover layer (ε_{r2} = 5 and ε_{r4} = 3, respectively). Wide band (Ka-band) simulations are produced (including an additive noise power of -50 dB) and the reconstructed reflectivity functions obtained from the RMA and AC-RMA algorithms are shown in Figure 9(a) and (b), respectively.

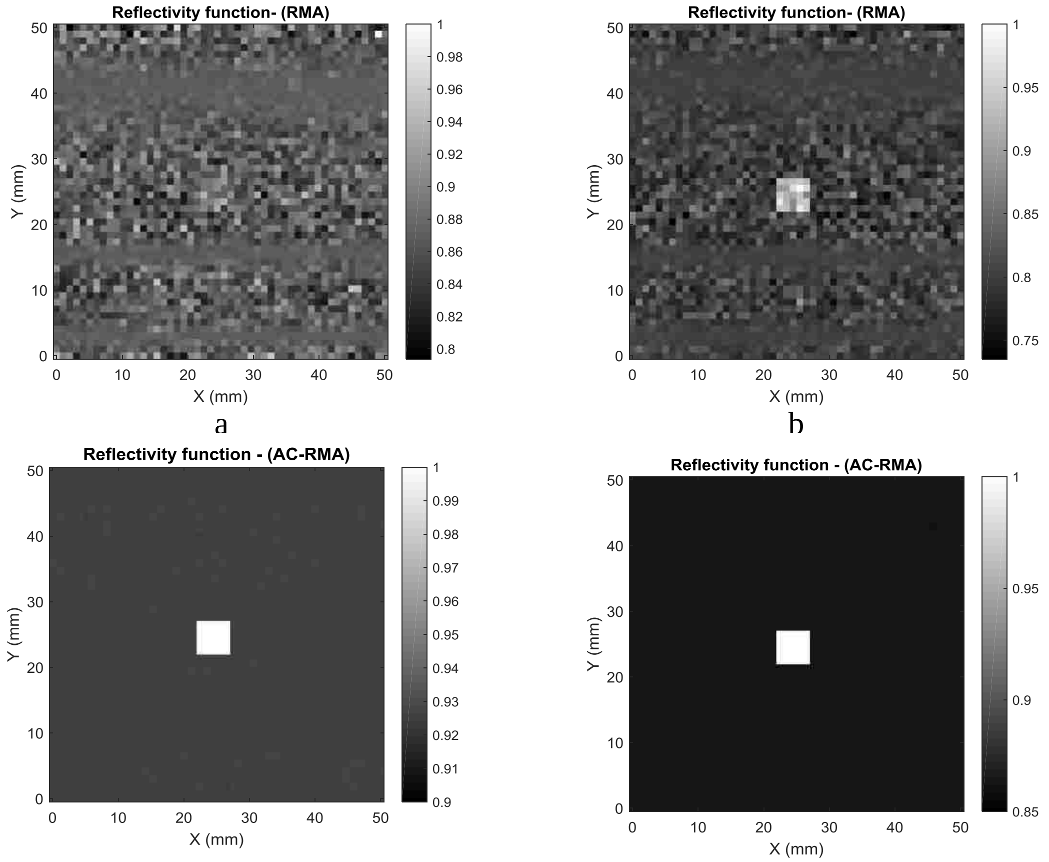

a b

c d

Figure 7. Reconstructed reflectivity function with -50 dB additive noise power when (a) $\varepsilon_{r\_target} = 24$, $\varepsilon_{r\_background} = 20$ and (b) $\varepsilon_{r\_target} = 40$, $\varepsilon_{r\_background} = 20$ using the RMA, and (c) $\varepsilon_{r\_target} = 24$, $\varepsilon_{r\_background} = 20$ and (d) $\varepsilon_{r\_target} = 40$, $\varepsilon_{r\_background} = 20$ using the AC-RMA.

Comparing these two images, Figure 9(a) (RMA) does not completely represent the contrast between areas of different permittivity (area with permittivities of ε_{r2} and ε_{r4}), while Figure 9(b) (AC-RMA) represents the different permtivities of the material more clearly. In the next simulation, the permittivity of the background is chosen as $\varepsilon_{r2} = 3$, less than that of the square target with $\varepsilon_{r4} = 5$, and permittivity of the cover layer remains the same as before. As seen in Figure 10(a), the reflectivity function reconstructed by the RMA algorithm is noisy (low image quality), but unlike the previous simulation (Figure 9(a)), the different permittivities are evident. However, the quality of the reflectivity function reconstructed by the AC-RMA algorithm in Figure 10(b) remains of high quality, meaning the AC-RMA can handle different contrasts between targets and layers regardless of their permittivity.

Next, the effect of the cover layer permittivity was studied. It is expected that the image quality of the reconstructed reflectivity function reduces for both algorithms when the permittivity of the cover layer (ε_{r1}) increases due to the reduction in the signal transmitted to the target (i.e., more is reflected by the cover layer). To this end, the reconstructed reflectivity functions obtained using both algorithms are studied for different values of ε_{r1} when all other parameters (additive noise power, imaging bandwidth, $\varepsilon_{r2,}$ and ε_{r4}) remain constant and equal to that of Figure 10. In the first simulation, $\varepsilon_{r1} = \varepsilon_{r4} = 5$, with the reconstructed reflectivity functions shown in Figure 11. As shown, when using the RMA algorithm, the target cannot be reconstructed. However, when using the AC-RMA algorithm, the target can be reconstructed with acceptable image quality to distinguish the different permittivity in the interference between first and second layer. The reconstructed reflectivity function for $\varepsilon_{r1} = 10$ is shown in Figure 12. In this case, similar to Figure 11(a), the target cannot be reconstructed by the RMA algorithm for $\varepsilon_{r1} = 10$. However, when using AC-RMA algorithm (Figure 12 (b)), the target can be reconstructed but the contrast between targets with different permittivities (i.e., the air gap and dielectric square) decreases. From these results, it can be concluded that the RMA algorithm has limited success for reconstruction of the reflectivity function of targets in layered media (ability to reconstruct in multilayer media for ε_{r1} less than ε_{r2} and ε_{r3}), while the AC-RMA algorithm can reconstruct the reflectivity function of the target regardless of the layer permittivity as long as the amplitude of the received signal is greater than the noise level.

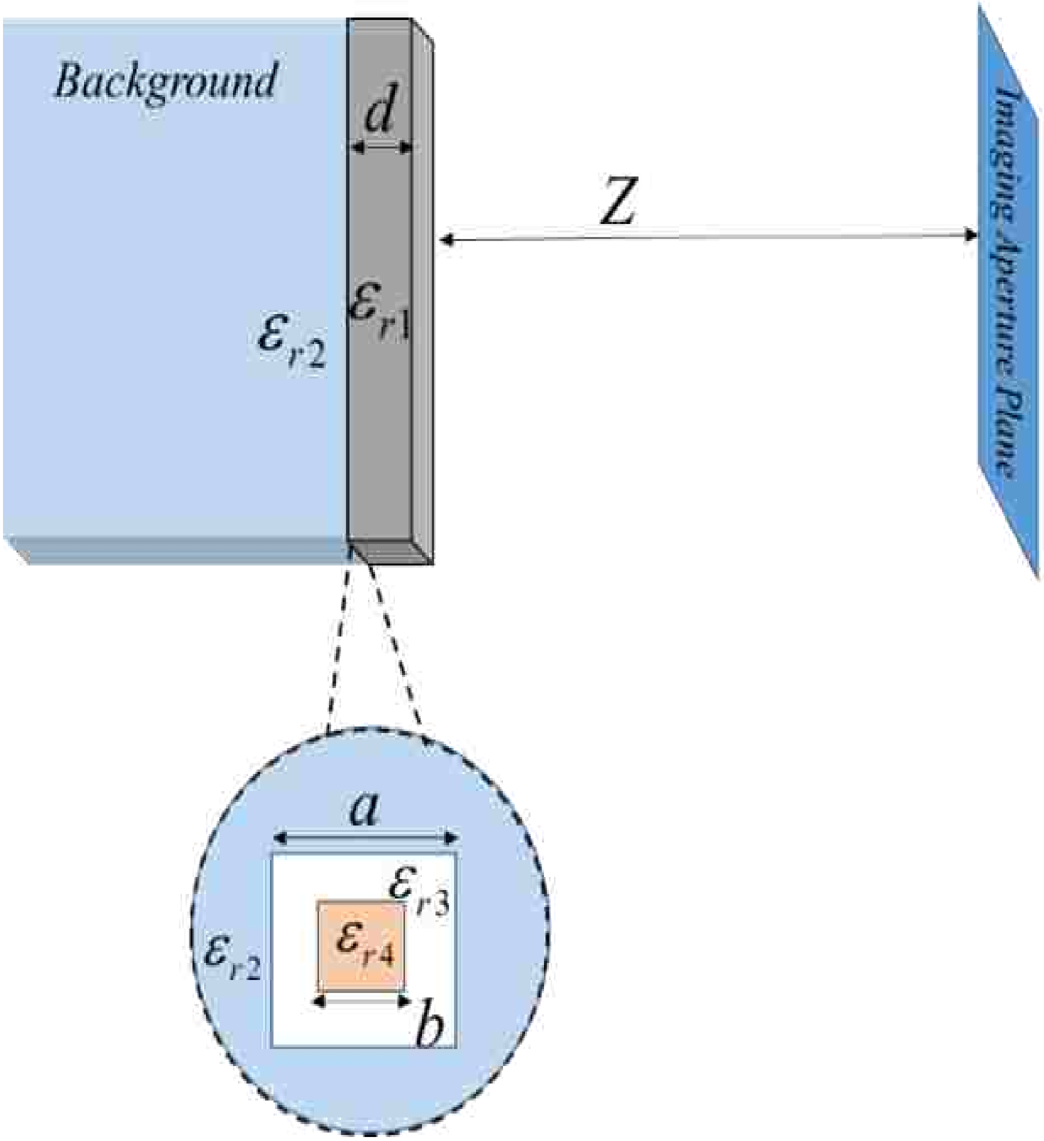

Figure 8. Schematic of the multilayer media imaging problem.

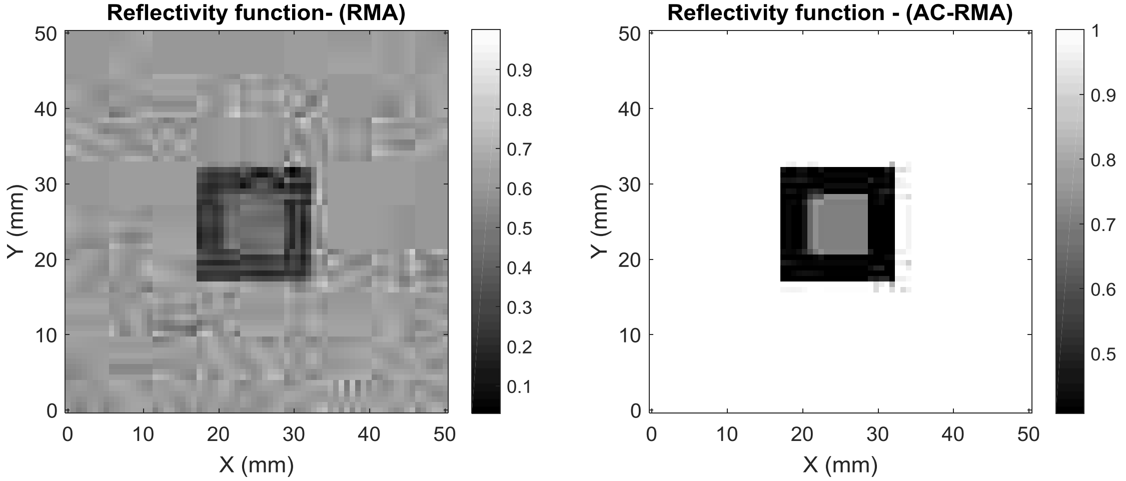

a

b

Figure 9. Wideband reconstructed reflectivity function at the boundary of the multilayer media with $\varepsilon_{r1} = 2.5$, $\varepsilon_{r2} = 5$, $\varepsilon_{r3} = 1$, and $\varepsilon_{r4} = 3$ for (a) RMA and (b) AC-RMA.

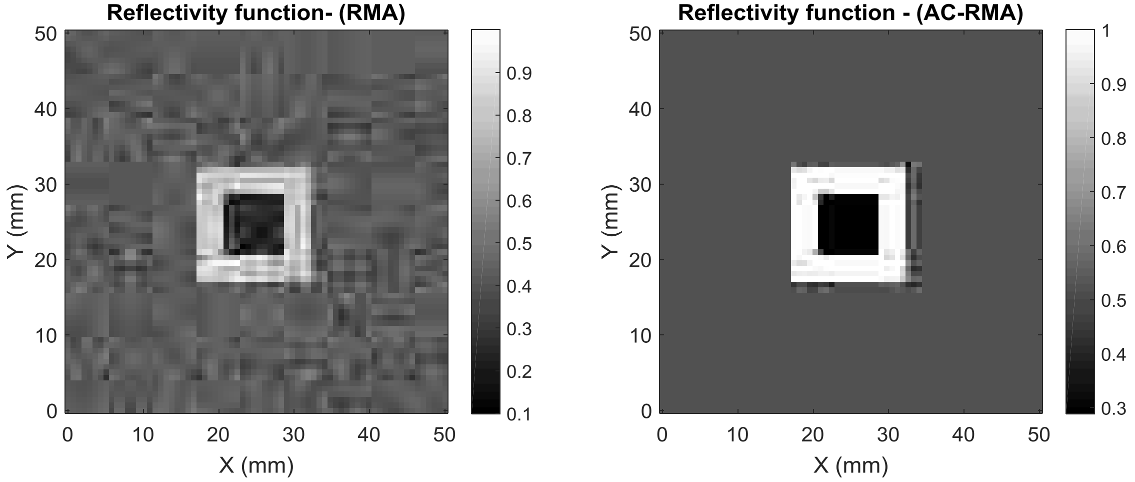

a

b

Figure 10. Wideband reconstructed reflectivity function at the boundary of the multilayer media with $\varepsilon_{r1} = 2.5$, $\varepsilon_{r2} = 3$, $\varepsilon_{r3} = 1$, and $\varepsilon_{r4} = 5$ for (a) RMA and (b) AC-RMA.

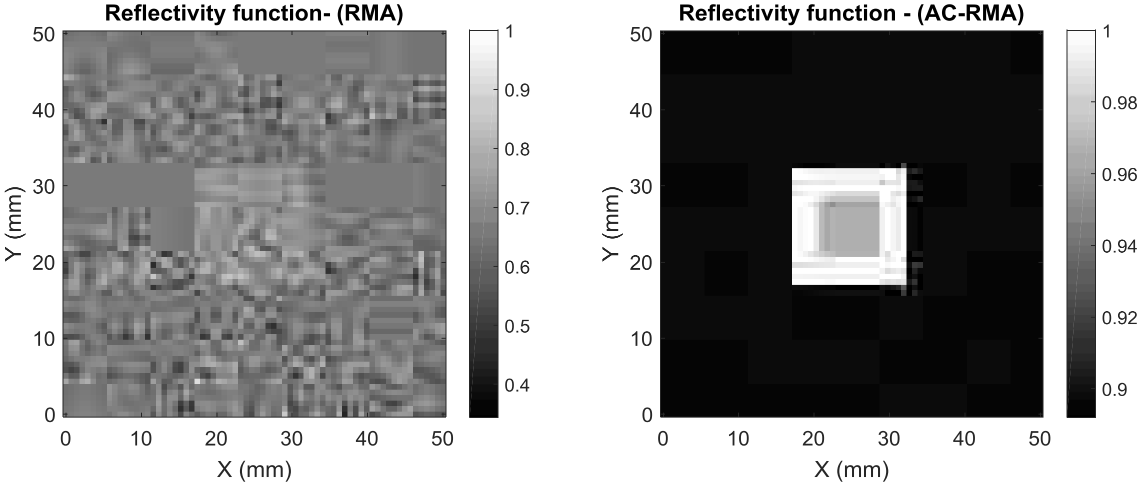

a b

Figure 11. Wideband reconstructed reflectivity function at the boundary of the multilayer media with $\varepsilon_{r1} = 5$, $\varepsilon_{r2} = 3$, $\varepsilon_{r3} = 1$, and $\varepsilon_{r4} = 5$ for (a) RMA and (b) AC-RMA.

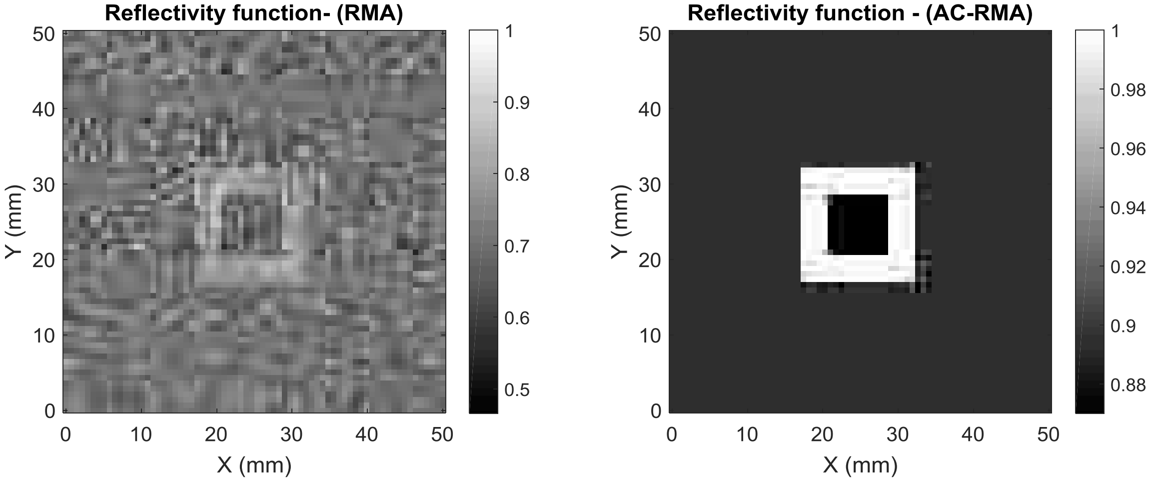

a b

Figure 12. Wideband reconstructed reflectivity function at the boundary of the multilayer media with $\varepsilon_{r1} = 10$, $\varepsilon_{r2} = 3$, $\varepsilon_{r3} = 1$, and $\varepsilon_{r4} = 5$ for (a) RMA and (b) AC-RMA.

Next, in order to extend this study to include realistic (lossy) dielectrics, the performance of both algorithms is considered for such materials as well. To this end, simulations were conducted for the scenario of Figure 10 but for a complex ε_{r1}. In Figure 13 and 14, the simulated reconstructed reflectivity function obtained using the RMA and AC-RMA algorithms are shown for low (0.08) and high (0.4) loss tangent (ε_{r1} = 2.5 - j0.20 and 2.5 – j1, respectively). As expected, since the amplitude effect in the matched filter of the RMA algorithm is not considered, the reflectivity function is not properly reconstructed by the RMA algorithm when there is loss present. However, with the AC-RMA algorithm, the reflectivity function of the target can be reconstructed in the presence of the lossy media.

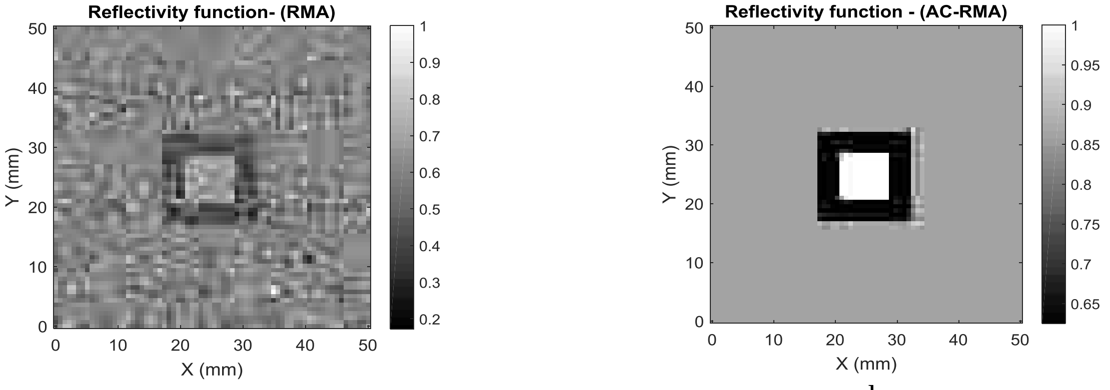

a b

Figure 13. Wideband reconstructed reflectivity function at the boundary of the multilayer media with ε_{r1} = 2.5-j0.20, ε_{r2} = 3, ε_{r3} = 1, and ε_{r4} = 5 for (a) RMA and (b) AC-RMA.

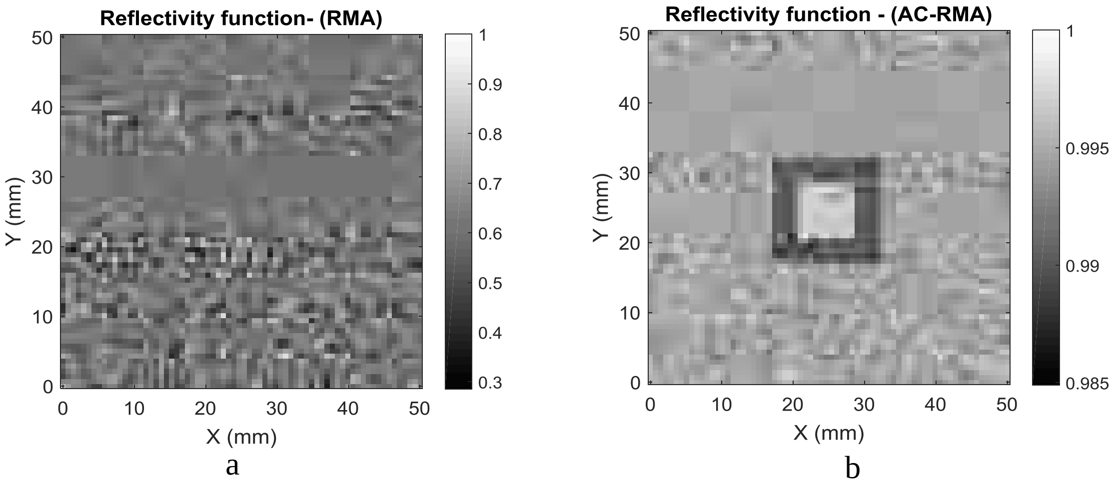

Figure 14. Wideband reconstructed reflectivity function at the boundary of the multilayer media with ε_{r1} = 2.5-j1, ε_{r2} = 3, ε_{r3} = 1, and ε_{r4} = 5 for (a) RMA and (b) AC-RMA.

As shown in Figure 13(b), for a loss tangent of 0.08 (low loss), the reconstructed reflectivity function has high contrast, but when the loss tangent increases, the contrast decreases (Figure 14(b)) due to low SNR resulting from these conditions (i.e., less received power as compared to low loss/lossless media). Moreover, due to the randomness in the added noise for different frequencies and locations within the Tx/Rx aperture plane, more accumulated noise is apparent in some areas of the image as compared to other areas.

Up to now, all simulations were implemented in MATLAB and the exact form of the backscattered signal, $s(x_t, y_t, x_r, y_r, k)$, was modeled and utilized to reconstruct the reflectivity function. Now, the image quality of the reconstructed reflectivity function obtained by the RMA and AC-RMA algorithms is compared with each other when the backscattered signal is obtained from full-wave simulation in CST Microwave Studio®. Since CST utilizes finite-difference time-domain modeling (FDTD) to solve the wave equations, at the interface between materials with different permittivities, a staircase grid is used to approximate the boundary [17]. This approximation degrades the accuracy of the calculated backscattered signal as will be shown below. Here, to replicate the experimental set up, two waveguide antennas at Ka-band (as Tx/Rx pair) with a 10 mm baseline length are located 40 mm from the dielectric target with $\varepsilon_{r\_target} = 3$ in the middle of the background with $\varepsilon_{r\_background} = 2.5$ (as illustrated in Figure 15). This Tx/Rx pair is used to simulate a 100 mm × 100 mm raster scan with a 2 mm step size, and the simulated transmission coefficient, S_{21} (between the Tx and Rx antennas), at each point is saved and exported to MATLAB software for translation of the backscattered signal from S- parameters as is outlined in [18], where S_{21} is equal to the spectral roundtrip Green function. Then, -75 dB noise power is added to the backscattered signal and the reflectivity function is reconstructed by the RMA and AC-RMA algorithms and shown in Figure 16. As can be seen in Figure 16(a), ghost indications appear around the reflectivity function reconstructed by the RMA algorithm and the overall image quality is less than that of the image reconstructed by the AC-RMA algorithm of Figure 16(b). However, at the boundary of the target and background in both images, fading is seen, which is attributed to the staircase grid approximation employed at the dielectric boundary [17]. Overall, the AC- RMA algorithm is able to reconstruct the reflectivity function better than RMA algorithm for low dielectric contrast.

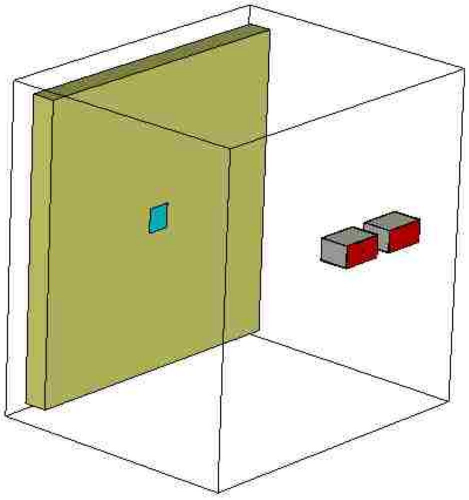

Figure 15. Imaging system setup for CST simulations.

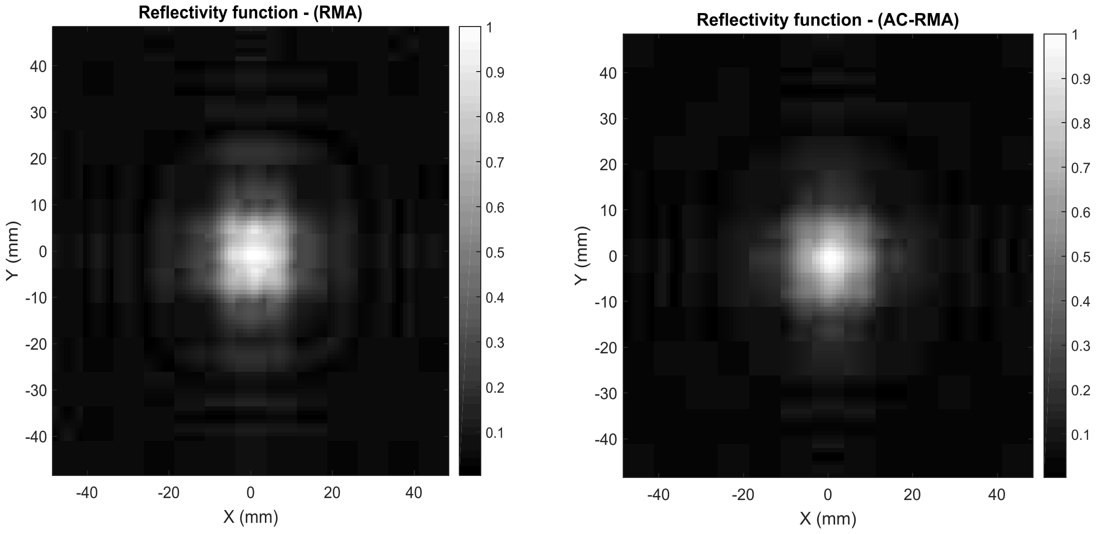

a

b

Figure 16. Reconstructed reflectivity function from CST simulations by (a) RMA and (b) AC-RMA.

4. EXPERIMENTAL RESULTS

In order to further illustrate the advantages offered by the AC-RMA algorithm, measurements were performed by using a cross-shaped 3D printed conductive polylactic acid (PLA) located in the center of a 80 mm x 80 mm non-conductive PLA block as shown in Figure 17(a). The complex permittivities of the conductive and non-conductive PLA are approximately 6-j10 and 3-j0 (i.e., negligible loss), respectivly [19]. The measurement setup is shown in Figure 17(b). The sample was located on a foam base and was scanned by two Ka-band waveguide antennas (the Tx/Rx pair) with a sampling step of 2 mm in both the *x* and *y* directions. The baseline length of the Tx/Rx pair is 22 mm, and the sample range is 40 mm. Here, both Tx and Rx antennas are connected to calibrated ports of an Anritsu MS4644A vector network analyzer (VNA). In the measurement setup, the Tx antenna was connected to port 1 of VNA, and the Rx antenna was connected to port 2. The backscattered signal from the illuminated sample is measured by the VNA as S_{21} and subsequently processed by the AC-RMA and RMA algorithms. As shown in Figure 18 (a), the contrast between the reconstructed image of the cross shaped conductive composite and the plastic background is less than that of the image reconstructed by the AC-RMA (Figure 18 (b)). Additionally, in Figure 18 (b), aside from the image of the cross-shaped conductive composite, the boundaries of the plastic sample are also represented clearly.

a

b

Figure 17. (a) Photograph of the sample and (b) scanning set up by Ka-band waveguide antennas as Tx/Rx pairs.

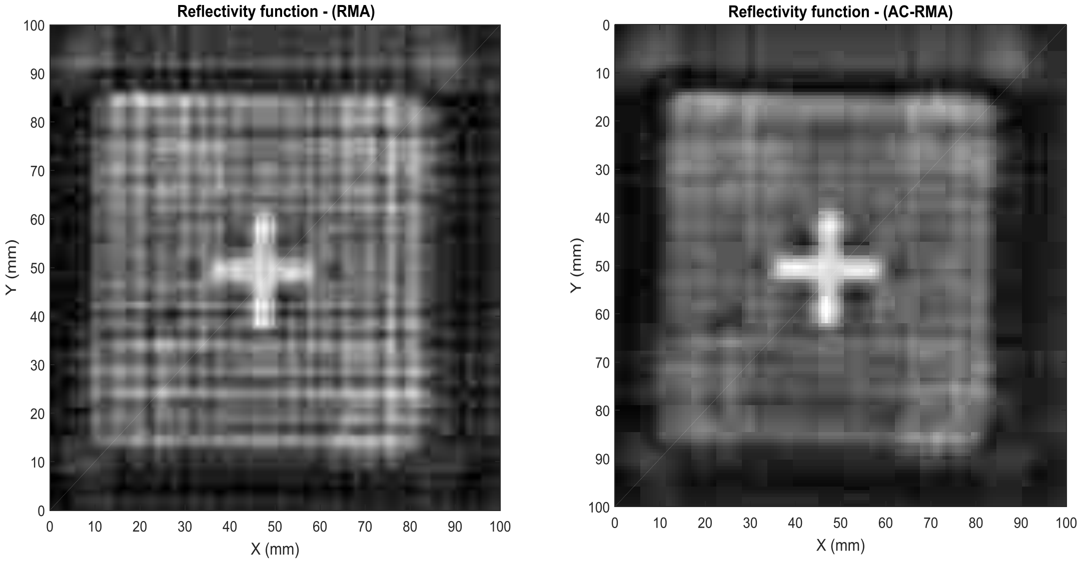

a

b

Figure 18. (a) RMA reconstructed reflectivity function and (b) AC-RMA reconstructed reflectivity function of the conductive composite inside plastic.

5. CONCLUSION

A bistatic range migration algorithm (the AC-RMA) which considers both phase and amplitude compensation has been developed and presented. By using the method of stationary phase, the matched filter of AC-RMA is developed and simulation and measurement results support the superiority of this algorithm as compared to previous works. Here, due to considering phase and amplitude compensation in the developed matched filter, the reconstructed reflectivity function becomes much less dependent on the contrast between the target and background, additive noise power and bandwidth of imaging system as compared to the RMA. Several simulations were conducted to compare the proposed AC-RMA to the RMA for various cases of dielectric contrast, high and low permittivity, multi-layered stuctures and lossy mediums. Additionally, measurements were conducted to compare these two algorithms. All the simualtions and measurmetns showed the supriority of AC-RMA in generating images of the targets in all cases.

APPENDIX

To find matched filter based on method of stationary phase (MSP), Equation (5) can be rewritten in form of Equation (1).

$$\begin{aligned} S(k_{xt},k_{xr},k_{yt},k_{yr},k) &= F(k_{xt},k_{xr},k_{yt},k_{yr},k)G(k_{xt},k_{yt},k)G(k_{xr},k_{yr},k) \\ &= F(k_{xt},k_{xr},k_{yt},k_{yr},k)\iint\iint[\frac{e^{(-jkR_t)}.e^{(-jkR_r)}}{(4\pi)^2 R_t.R_r} e^{-j(k_{xt}x_t+k_{xr}x_r+k_{yt}y_t+k_{yr}y_r)}]dx_t dy_t dx_r dy_r \end{aligned} \tag{1}$$

Integral of Equation (13) can be evaluated asymptotically by using the method of stationary phase (MSP) [20]. This method provides an analytical solution to integrals of the form:

$$N(K)=\iint\limits_R g(x,y)\,\mathrm{e}^{jK\mu(x,y)}\,dxdy \tag{2}$$

$$g(x_t,y_t,x_r,y_r)=\frac{1}{R_tR_r} \tag{3}$$

$$K\mu(x_t,y_t,x_r,y_r)=\Phi(x_t,y_t,x_r,y_r)=-kR_t-kR_r-k_{xt}x_t-k_{xr}x_r-k_{yt}y_t-k_{yr}y_r \tag{4}$$

$$\begin{aligned}
&\frac{d\Phi}{dx_t}\Big|_{x_t^0}=-kx_t-\frac{k.(x_t^0-x)}{R_t(x_t^0,y_t^0)}=0,\\
&\frac{d\Phi}{dx_r}\Big|_{x_r^0}=-kx_r-\frac{k.(x_r^0-x)}{R_r(x_r^0,y_r^0)}=0,\\
&\frac{d\Phi}{dy_t}\Big|_{y_t^0}=-ky_t-\frac{k.(y_t^0-y)}{R_t(x_t^0,y_t^0)}=0,\\
&\frac{d\Phi}{dy_r}\Big|_{y_r^0}=-ky_r-\frac{k.(y_r^0-y)}{R_r(x_r^0,y_r^0)}=0
\end{aligned} \tag{5}$$

$$\begin{aligned}
&R^0_t=\frac{-k.z}{\sqrt{k^2-k_{xt}{}^2-k_{yt}{}^2}}=\frac{-k.z}{k_{zt}}\\
&R^0_r=\frac{-k.z}{\sqrt{k^2-k_{xr}{}^2-k_{yr}{}^2}}=\frac{-k.z}{k_{zr}}\\
&x_t^0=\frac{k_{zt}x-k_{xt}z}{k_{zt}},\,x_r^0=\frac{k_{zr}x-k_{xr}z}{k_{zr}}\\
&y_t^0=\frac{k_{zt}y-k_{yt}z}{k_{zt}},\,y_r^0=\frac{k_{zr}y-k_{yr}z}{k_{zr}}
\end{aligned} \tag{6}$$

Now based on Taylor series, phase function can be written as:

$$\Phi(x_t, y_t, x_r, y_r) = \Phi(x_t^0, y_t^0, x_r^0, y_r^0) + \frac{1}{2}\begin{bmatrix} \Phi_{xtxt}(x_t^0, y_t^0, x_r^0, y_r^0)(x_t - x_t^0)^2 \\ +\Phi_{xrxr}(x_t^0, y_t^0, x_r^0, y_r^0)(x_r - x_r^0)^2 \\ +\Phi_{ytyt}(x_t^0, y_t^0, x_r^0, y_r^0)(y_t - y_t^0)^2 \\ +\Phi_{yryr}(x_t^0, y_t^0, x_r^0, y_r^0)(y_r - y_r^0)^2 \\ +2\Phi_{xtyt}(x_t^0, y_t^0, x_r^0, y_r^0)(x_t - x_t^0)(y_t - y_t^0) \\ +2\Phi_{xryr}(x_t^0, y_t^0, x_r^0, y_r^0)(x_r - x_r^0)(y_r - y_r^0) \end{bmatrix} \tag{7}$$

Where:

$$\begin{aligned} \Phi_{xtxt}(x_t^0, y_t^0, x_r^0, y_r^0) &= -\frac{k_{zt}}{z} - \frac{k_{xt}.k_{zt}^2}{k^2.z^2} \\ \Phi_{ytyt}(x_t^0, y_t^0, x_r^0, y_r^0) &= -\frac{k_{zt}}{z} - \frac{k_{yt}.k_{zt}^2}{k^2.z^2} \\ \Phi_{xrxr}(x_t^0, y_t^0, x_r^0, y_r^0) &= -\frac{k_{zr}}{z} - \frac{k_{xr}.k_{zr}^2}{k^2.z^2} \\ \Phi_{yryr}(x_t^0, y_t^0, x_r^0, y_r^0) &= -\frac{k_{zr}}{z} - \frac{k_{yr}.k_{zr}^2}{k^2.z^2} \end{aligned} \tag{8}$$

Finally, by substituting equation (19) in (13):

$$\begin{aligned} &G(k_{xt}, k_{yt}, k_{xr}, k_{yr}, k) = G(k_{xt}, k_{yt}, k)G(k_{xr}, k_{yr}, k) = \\ &\left[\frac{\mathrm{e}^{j\Phi(x_t^0, x_r^0, y_t^0, y_r^0)}}{(4\pi)^2 R_t(x_t^0, y_t^0) R_r(x_r^0, y_r^0)}\right]. \\ &\iint\iint \mathrm{e}^{j\begin{pmatrix} \Phi_{xtxt}(x_t^0, y_t^0, x_r^0, y_r^0)(x_t - x_t^0)^2 \\ +\Phi_{xrxr}(x_t^0, y_t^0, x_r^0, y_r^0)(x_r - x_r^0)^2 \\ +\Phi_{ytyt}(x_t^0, y_t^0, x_r^0, y_r^0)(y_t - y_t^0)^2 \\ +\Phi_{yryr}(x_t^0, y_t^0, x_r^0, y_r^0)(y_r - y_r^0)^2 \\ +2\Phi_{xtyt}(x_t^0, y_t^0, x_r^0, y_r^0)(x_t - x_t^0)(y_t - y_t^0) \\ +2\Phi_{xryr}(x_t^0, y_t^0, x_r^0, y_r^0)(x_r - x_r^0)(y_r - y_r^0) \end{pmatrix}} dx_t dy_t dx_r dy_r \end{aligned} \tag{9}$$

$$G(k_{xt},k_{yt},k_{xr},k_{yr},k)=\left[\frac{\mathrm{e}^{j\Phi(x_t^0,x_r^0,y_t^0,y_r^0)}}{(4\pi)^2R_t(x_t^0,y_t^0)R_r(x_r^0,y_r^0)}.\mathrm{e}^{(j\pi/4)}\right].\left(\begin{array}{l}8a^2b\sqrt{\dfrac{2\pi}{\left|\Phi_{y_ry_r}(x_r^0,y_r^0)\right|}}+8b^2a\sqrt{\dfrac{2\pi}{\left|\Phi_{x_rx_r}(x_r^0,y_r^0)\right|}}+\\ 8a^2b\sqrt{\dfrac{2\pi}{\left|\Phi_{y_ty_t}(x_t^0,y_t^0)\right|}}+8b^2a\sqrt{\dfrac{2\pi}{\left|\Phi_{x_tx_t}(x_t^0,y_t^0)\right|}}\\ +4(a-x_t^0)Si((a-x_t^0)(b-y_t^0)\Phi_{y_tx_t}(x_t^0,y_t^0))+\\ 4(a-x_r^0)Si((a-x_r^0)(b-y_r^0)\Phi_{y_rx_r}(x_r^0,y_r^0))\end{array}\right) \tag{10}$$

REFERENCES

R. Zoughi, "Microwave nondestructive testing: Theories and applications", Proc. *IEEE International Advances in Nondestructive Testing (IANDT)*, vol. 15, pp. 255-288, 1990.

J. T. Case, M. T. Ghasr, R. Zoughi, "Nonuniform manual scanning for rapid microwave nondestructive evaluation imaging", *IEEE Trans. Instrum. Meas.*, vol. 62, pp. 1250-1258, May 2013.

L. Cutrona, E. Leith, L. Porcello, and W. Vivian, “On the application of coherent optical processing techniques to synthetic aperture radar,” *Proc. IEEE*, vol. 54, p. 1026, 1966.

X. Mao, D. Zhu, Z. Zhu, "Polar format algorithm wavefront curvature compensation under arbitrary radar flight path", *IEEE Geosci. Remote Sens. Lett.* vol. 9, no. 3, pp. 526-530, May 2012.

D. Sheen, D. McMakin, T. E. Hall, "Three-dimensional millimeter-wave imaging for concealed weapon detection", *IEEE Trans. MTT*, vol. 49, no. 9, pp. 1581-1592, 2001.

D. Ausherman, A. Kozma, J. Walker, H. Jones, and E. Poggio, “Developments in radar imaging,” *IEEE Trans. Aerosp. Electron. Syst.*, vol. 20, p. 363, July 1984.

J. M. Lopez-Sahcnez, J. Fortuny-Guash, "3D radar imaging using range migration techniques", *IEEE Trans. Antennas Propagat.*, vol. 48, pp. 728-737, May 2000.

F. Gumbmann, P. H. Tran, J. Weinzierl, L.-P. Schmidt, "Advanced broadband millimeter-wave characterization techniques of dielectrics", *Proc. ECNDT*, 2006.

J. Gao, B. Shanker, "Time domain Weyl's identity and the causality trick based formulation of the time domain periodic Green's function", *IEEE Trans. Antennas Propag.*, vol. 55, no. 6, pp. 1656-1666, Jun. 2007.

J. Gao, B. Shanker, "Time domain Weyl's identity and the causality trick based formulation of the time domain periodic Green's function", *IEEE Trans. Antennas Propag.*, vol. 55, no. 6, pp. 1656-1666, Jun. 2007.

D. A. Garren, "SAR Focus Theory of Complicated Range Migration Signatures Due to Moving Targets." *IEEE Geoscience and Remote Sensing Letters*. 2018.

H. T. Xie, D. X. An, X. T. Huang, Z. M. Zhou, "Fast time-domain imaging in elliptical polar coordinate for general bistatic VHF/UHF ultra-wideband SAR with arbitrary motion", *IEEE J. Sel. Topics Appl. Earth Observ.*, vol. 8, no. 2, pp. 879-895, Feb. 2015.

M. Soumekh, "Bistatic synthetic aperture radar inversion with application in dynamic object imaging", *IEEE Trans. Signal Processing*, vol. 39, pp. 2044-2055, Sept. 1991.

R. Zhu, J. Zhou, G. Jiang, Q. Fu, "Range Migration Algorithm for Near-Field MIMO-SAR Imaging", *IEEE Geoscience and Remote Sensing Letters*., vol. 14, pp. 2280 - 2284, Dec. 2017.

R. Zhu, J. Zhou, G. Jiang, Q. Fu, "Range Migration Algorithm for Near-Field MIMO-SAR Imaging", *IEEE Geoscience and Remote Sensing Letters*., vol. 14, pp. 2280 - 2284, Dec. 2017.

Z. Manzoor, M. T. Ghasr, K.M. Donnell, "Image distortion characterization due to equivalent monostatic approximation in near field bistatic SAR imaging", *Instrumentation and Measurement Technology Conference (I2MTC), 2017 IEEE International*., pp. 1-5, May 2017.

M. Fallahpour, J. T. Case, M. T. Ghasr, R. Zoughi, "Piecewise and Wiener filter-based SAR techniques for monostatic microwave imaging of layered structures", *IEEE Trans. Instrum. Meas.*, vol. 62, no. 1, pp. 282-294, Jan. 2014.

T. H. Kim, R. James, R. M. Narayanan. "High-resolution nondestructive testing of multilayer dielectric materials using wideband microwave synthetic aperture radar imaging." *Nondestructive Characterization and Monitoring of Advanced Materials, Aerospace, and Civil Infrastructure 2017*. vol. 10169. International Society for Optics and Photonics, 2017.

P. A. Tirkas, C. A. Balanis, "Finite-difference time-domain technique for antenna radiation", *1990 IEEE Antennas and Propagation Symp. Dig.*, vol. I, pp. 14-17, 1990-May-7-11.

S. Arslanagic et al., "A review of the scattering-parameter extraction method with clarification of ambiguity issues in relation to metamaterial homogenization", *IEEE Antennas Propag. Mag.*, vol. 55, no. 2, pp. 91-106, Apr. 2013.

Z. Manzoor, M. T. Ghasr, K.M. Donnell, "Microwave characterization of 3D printed conductive composite materials," 2018 *IEEE International Instrumentation and Measurement Technology Conference (I2MTC)*, Houston, TX, 2018, pp. 1-5.

N. G. Van Kampen, "The method of stationary phase and the method of Fresnel zones", *Physica*, vol. 24, pp. 437-444, 1958.

SECTION

2. CONCLUSIONS AND RECOMMENDATIONS

2.1. CONCLUSIONS

The overarching objective of this work was to design, prototype and test an innovative millimeter wave imaging system that operates in the frequency range of 33-35 GHz and is capable of producing rapid images of various diverse scenes. Here, the ability to randomly and electronically activate some of the (2D) imaging array elements or a portion of the imaging array were included in this system design. To this end, in paper I, a 1D non-uniform switched array, employing an antipodal Vivaldi antenna as the array element, was fabricated and used for imaging. In the designed non-uniform array, the baseline length of transmitter/receiver pairs varies between one and two wavelengths of the mid-band frequency. This 1D array was used to provide electronic scanning in one dimension while it was moved in the other dimension to generate 2D SAR images. The obtained SAR images of the imaged targets had minor image quality degradation (as compared to a single raster scanned result). Overall, this design can be extended to a 2D array for real-time imaging without the need for raster scanning.

Designing sparse imaging array with random distribution provides the potential to incorporate several different fast imaging algorithms such as the non-uniform ω-k SAR. A combination of the computationally efficient monostatic ω-k SAR for near field 3D SAR imaging and the high dynamic range bistatic measurements are used to create images using the array. This combinationm results is image distortion caused by using an equivalent monostatic imaging algorithm for bistatic measurements which is studied in paper II. In order to fully investigate the image distortion that results from the application of a monostatic model to bistatic SAR measurements, additional simulations and measurements were conducted for different layouts of Tx/Rx pairs, therein simulating raster scanning and non-uniform imaging arrays. Studies showed that the effect of the number of sampling points on image quality is more significant in near field imaging as compared to far field imaging. Moreover, by applying phase compensation to minimize phase differences between bistatic measurement and monostatic model, the image error is improved.

Finally, in paper III, the AC-RMA which considers both phase and amplitude compensation has been developed. By using method of stationary phase, the matched filter of AC-RMA is derived and simulation and measurement results support the superiority of the developed algorithm compared to the traditional RMA. Here, due to considering phase and amplitude compensation in the developed matched filter, reconstructed reflectivity function is independent of contrast between target and background, additive noise power and bandwidth of imaging system. In addition, targets with different dielectric properties can be distinguished in lossy multilayer media.

2.2. RECOMMENDATIONS

Despite of applied modifications in designing sparse imaging array, still image quality can be improved by considering some recommendations that are discussed here.

2.2.1. Phase Compensation. For future work, a new correction method can be investigated to compensate phase difference between monostatic model and bistatic configuration for 2D sparse imaging array. As discussed in paper II, by applying proposed phase compensation method on 2D non-uniform array, the image error only improves slightly due to the extreme sparsity of the array (limited number of sampling points). However, 2D sparse array is preferred for imaging purpose due to providing real time image reconstruction. Hence, by developing new correction method usable for 2D sparse imaging array, equivalent monostatic model can be used for bistatic measurement with negligible image distortion.

2.2.2. Array Density. As discussed in [21], for low density of imaging aperture (less than 5% of under-sampling rate compared to ideal sampling), image quality degrades dramatically. Hence, future designs of imaging arrays should employ number of spatial sampling points greater than 5% of ideal sampling case dictated by Nyquist Criteria.

2.2.3. Imaging System's Bandwidth. The designed imaging system has a bandwidth of 2 GHz. This limited bandwidth was mainly due to the limitations in the available components (mainly the switches and amplifiers) beyond 35 GHz. Due to this limited bandwidth, the 3D imaging ability of designed array is limited.

It is recommended that future design be able to utilize larger bandwidth. This is due to the orthogonality of signals at different frequencies, which provides constructive interference at target location and destructive interference at other location reducing clutter and enhancing overall image SNR. This is important when the clutter is due to aliasing or similar image artifacts, since the spatial locations of aliasing artifacts is frequency dependent and therefore overall aliasing in the image is reduced when wideband images are accumulated.

2.2.4. Antenna Design. The antipodal Vivaldi antenna is a low-cost, wideband solution and provides a direct integration with the RF PCBs. However, the antipodal

Vivaldi antennas on a thin RF PCBs are not mechanically reliable and represent another point of failure. To this end, radome enclosure for the operating frequency can be designed for the proposed antenna in paper I to reach mechanically robust hardware without disturbing radiation pattern of the designed antenna.

BIBLIOGRAPHY

1. J. T. Case, F. L. Hepburn, R. Zoughi, "Inspection of Spray on Foam Insulation (SOFI) Using Microwave and Millimeter Wave Synthetic Aperture Focusing and Holography," in Instrumentation and Measurement Technology Conference, 2006. IMTC 2006. Proceedings of the IEEE, 2006, pp. 2148-2153.

2. J. T. Case, M. T. Ghasr, R. Zoughi, "Optimum Two-Dimensional Uniform Spatial Sampling for Microwave SAR-Based NDE Imaging Systems," IEEE Trans. Instrum. Meas., vol. 60, pp. 3806-3815, 2011.

3. J. T. Case, S. Kharkovsky, R. Zoughi, and F. Hepburn, "High Resolution Millimeter Wave Inspecting of the Orbiter Acreage Heat Tiles of the Space Shuttle," in Instrumentation and Measurement Technology Conference Proceedings, 2007. IMTC 2007. IEEE, 2007, pp. 1-4.

4. M. T. Ghasr, Kuang P. Ying ,Reza Zoughi," SAR imaging for inspection of metallic surfaces at millimeter wave frequencies", Instrumentation and Measurement Technology Conference (I2MTC) Proceedings, 2014 IEEE International,july 2014.

5. M. Pastorino, Microwave imaging vol. 208: John Wiley & Sons, 2010.

6. D. M. Sheen, D. L. McMakin, and T. E. Hall, "Three-dimensional millimeter-wave imaging for concealed weapon detection," IEEE Trans. Microw. Theory Tech.vol. 49, pp. 1581-1592, 2001.

7. M. T. Ghasr, M. A. Abou-Khousa, S. Kharkovsky, R. Zoughi, D. Pommerenke, "Portable real-time microwave camera at 24 GHz", *IEEE Trans. Antennas Propag.*, 2011.

8. D.M. Sheen, D.L. McMakin and T.E. Hall, ""Three-dimensional millimeter-wave imaging for concealed weapon detection," *IEEE Trans. Microwave Theory and Techniques*, vol. 49, No.9, Sept. 2001.

9. P.F. Goldsmith, C.-T. Hsieh, G.R. Huguenin, J. Kapitzky, E.L. Moore, "Focal plane imaging systems for millimeter wavelengths," IEEE Trans. on *Microwave Theory and Techniques*, vo1.41, no.10, pp.1664-1675, Oct 1993.

10. S. Clark, C. Martin, V. Kolinko, J. Lovberg, P.J. Costianes, "A real-time wide field ofview passive millimeter-wave imaging camera," *Proceedings. 32nd Applied Imagery Pattern Recognition Workshop,* vol., no., pp. 250-254, 15-17 Oct. 2003.

11. Committee on Assessment of Security Technologies for Transportation,"Assessment of Millimeter-Wave and Terahertz Technology for Detection and Identification of Concealed Explosives and Weapons," Washington, D.C: *The National Academic Press*. 2007.

12. Y. Wu, Y. Huang, X.Wu, “A equivalent monostatic imaging algorithm for bistatic synthetic aperture radar,” Synthetic Aperture Radar, 2007. APSAR 2007. 1st Asian and Pacific Conference on, January 2008.

13. Ender, J., I. Walterscheid, A. Brenner, “New aspects of bistatic SAR: Processing and experiments," Proc. of IGARSS, 1758-1762, 2004.

14. Z.Wu, X. Zhang, X.Wu,” A Novel Wavenumber Domain Algorithm for Bistatic SAR Imaging Based on Equivalent Monostatic Model”, Progress In Electromagnetics Research M, Vol. 45, 113–121, 2016.

15. R. Solimene, F. Soldovieri, G. Prisco, "'A Mu1tiarray Tomographic Approach for Through-Wall Imaging," IEEE Trans. on Geoscience and Remote Sensing, vol.46, no.4, pp.l 192-1199, April 2008.

16. J. T. Case, M. T. Ghasr, R. Zoughi, "Optimum 2-D nonuniform spatial sampling for microwave SAR-based NDE imaging systems", IEEE Trans. Instrum. Meas., vol. 61, no. 11, pp. 3072-3083, Nov. 2012.

17. L. Wang, A. M. Al-Jumaily, R. Simpkin, "Investigation of antenna array configurations using far-field holographic microwave imaging technique", Progress In Electromagnetics Research M, vol. 42, pp. 1-11, 2015.

18. Y. T. Lo, "A mathematical theory of antenna arrays with randomly spaced elements", *IEEE Trans. Antennas Propag.*, vol. AP-12, no. 3, pp. 257-268, May 1964.

19. M.Soumekh, “Bistatic Synthetic Aperture Radar Inversion with Application in Dynamic Object Imaging,” IEEE Transactions on Signal Processing Vol.39, pp.2044 - 2055, Sep 1991.

20. Y. S. Amrullah, K. Paramayudha and Y. Wahyu, "Enhancement performance tapered slot vivaldi antenna for weather radar application," *2016 International Seminar on Intelligent Technology and Its Applications (ISITIA)*, Lombok, pp. 329-332, 2016.

21. X. Yang, Y. R. Zheng, M. T. Ghasr and K. M. Donnell, "Microwave Imaging From Sparse Measurements for Near-Field Synthetic Aperture Radar," in IEEE Transactions on Instrumentation and Measurement, vol. 66, no. 10, pp. 2680-2692, Oct. 2017.

VITA

Zahra Manzoor was born in Tehran, Iran. She received her B.Sc. degree in Electrical Engineering from University of Tabriz, Tabriz, Iran in 2009 and M.Sc. degree from Amir Kabir University of Technology, Tehran, Iran, in 2013. She joined the Applied Microwave Nondestructive Testing Laboratory (amntl) at the Missouri University of Science and Technology in Spring 2016 as a Ph.D. student. In December 2019, she received her Ph.D. in Electrical Engineering from Missouri University of Science and Technology. Her research interests included a microwave and millimeter-wave imaging, optical imaging, topological and non-reciprocal photonic, scattering, material characterization, electromagnetic compatibility and RF circuit design.